JACS
JOURNAL OF THE AMERICAN CHEMICAL SOCIETY
pubs.acs.org/JACS
Article

Ethene Hydroformylation Catalyzed by Rhodium Dispersed with Zinc or Cobalt in Silanol Nests of Dealuminated Zeolite Beta

Liang Qi, Sonali Das, Yanfei Zhang, Danna Nozik, Bruce C. Gates, and Alexis T. Bell*

Cite This: J. Am. Chem. Soc. 2023, 145, 2911−2929
Read Online

ABSTRACT: Catalysts for hydroformylation of ethene were prepared by grafting Rh into nests of ≡SiOZn−OH or ≡SiOCo−OH species prepared in dealuminated BEA zeolite. X-ray absorption spectra and infrared spectra of adsorbed CO were used to characterize the dispersion of Rh. The Rh dispersion was found to increase markedly with increasing M/Rh (M = Zn or Co) ratio; further increases in Rh dispersion occurred upon use for ethene hydroformylation catalysis. The turnover frequency for ethene hydroformylation measured for a fixed set of reaction conditions increased with the fraction of atomically dispersed Rh. The ethene hydroformylation activity is 15.5-fold higher for M = Co than for M = Zn, whereas the propanal selectivity is slightly greater for the latter catalyst. The activity of the Co-containing catalyst exceeds that of all previously reported Rh-containing bimetallic catalysts. The rates of ethene hydroformylation and ethene hydrogenation exhibit positive reaction orders in ethene and hydrogen but negative orders in carbon monoxide. *In situ* IR spectroscopy and the kinetics of the catalytic reactions suggest that ethene hydroformylation is mainly catalyzed by atomically dispersed Rh that is influenced by Rh−M interactions, whereas ethene hydrogenation is mainly catalyzed by Rh nanoclusters. *In situ* IR spectroscopy also indicates that the ethene hydroformylation is rate limited by formation of propionyl groups and by their hydrogenation, a conclusion supported by the measured H/D kinetic isotope effect. This study presents a novel method for creating highly active Rh-containing bimetallic sites for ethene hydroformylation and provides new insights into the mechanism and kinetics of this process.

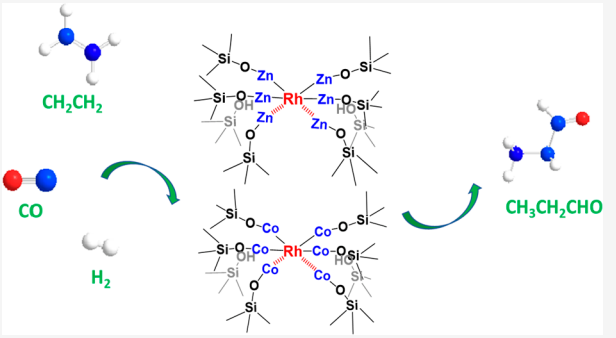

INTRODUCTION

Alkene hydroformylation to produce aldehydes is one of the most important homogeneously catalyzed industrial processes, with an annual global capacity of more than 10 million tons.[1−3] Rhodium complexes incorporating phosphine or phosphite ligands are widely used catalysts, because they exhibit both high activity and selectivity.[4−8] However, as is typical in homogeneous catalytic processes, catalyst separation and recycling are challenging, and rhodium reclamation and proper disposal of phosphine-containing wastes contribute significantly to the process cost.[1,9−11] These limitations have motivated interest in solid hydroformylation catalysts. These catalysts include anchored Rh complexes containing organophosphines,[1,2,12,13] Rh grafted to phosphine-modified porous organic polymers,[14−19] solid Rh phosphides,[4,20−22] and Rh complexes contained in supported ionic liquids.[23,24] Notwithstanding these advances, most of the reported catalysts still require phosphine ligands, which are expensive and both air- and moisture-sensitive, resulting in significant product−catalyst separation challenges.[21,25,26]

Another approach to creating Rh sites that are active for alkene hydroformylation involves dispersing Rh atoms on metal oxide supports, as either monometallic[10,27−30] or bimetallic species. The interactions of Rh atoms with nonprecious metals, such as Fe,[31,32] Mo,[33] Co,[9,12,20,34−36] Zn,[37,38] Re,[27,28] and W,[39] have facilitated the dispersion of Rh atoms having high hydroformylation activities. For example, Huang et al.[37] have reported that rhodium−zinc nanoparticles with diameters of 9.6 ± 0.6 nm supported on SBA-15 exhibit high activities for styrene hydroformylation. Chen et al.[9] have reported that rhodium stably dispersed with cobalt on mesoporous MCM-41 exhibits a turnover frequency (TOF) of ca. 270 h^{-1} for ethylene hydroformylation at 1 bar and 453 K. In related work, Ro et al.[28] have reported that ReO_x species supported on γ-Al_2O_3 stabilize a high dispersion of rhodium and produce a highly active and selective catalyst for ethene hydroformylation. Working with a feed containing C_2H_4, H_2, and CO in a 1:1:1 molar ratio, these authors found that rhodium supported on ReO_x on γ-Al_2O_3 exhibits a propanal formation turnover frequency (TOF) of ca. 5 h^{-1}. In a

Received: October 19, 2022
Published: January 30, 2023

https://doi.org/10.1021/jacs.2c11075
J. Am. Chem. Soc. 2023, 145, 2911−2929

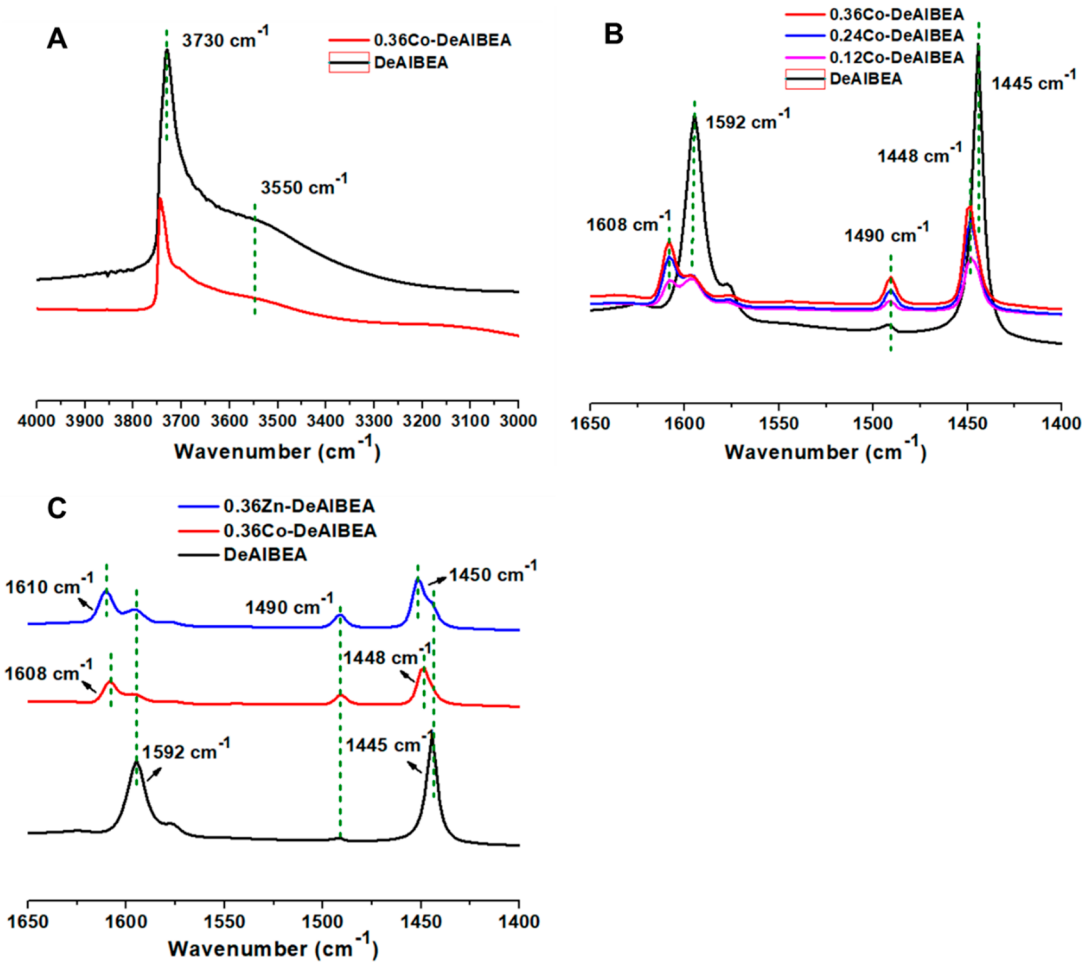

Figure 1. (A) Comparison of the IR spectra of the hydroxyl stretching region for DeAlBEA and 0.36Co-DeAlBEA. (B) IR spectra of adsorbed pyridine on DeAlBEA, 0.12Co-, 0.24Co-; and 0.36Co-DeAlBEA. (C) Comparison of IR spectra of adsorbed pyridine on DeAlBEA, 0.36Co-DeAlBEA, and 0.36Zn-DeAlBEA.

subsequent study the same group reported that atomically dispersed Rh−WO_x pairs supported on γ-Al_2O_3 catalyze the hydroformylation of a 1:1:1 mixture of C_2H_4, H_2, and CO at 403 K with a propanal TOF of ca. 21 h^{-1} and a propanal selectivity of ca. 90%.[39]

The preceding examples show that isolation of Rh atoms in bimetallic nanoparticles or by interaction with supported metal oxide species can produce active and selective sites for alkene hydroformylation. We posit that a central challenge is to understand how Rh can be maintained in a highly dispersed state and how the nonprecious elements used to maintain Rh in such a state affect its activity and selectivity for alkene hydroformylation.[40−45] Our approach to addressing this challenge was stimulated by our recent work showing that nests of four to six ≡SiOZnOH Lewis acid sites produced by introducing Zn into silanol nests of dealuminated zeolite Beta can anchor Pt as isolated atoms.[46,47] After reduction, characterization by X-ray absorption spectroscopy (XAS) revealed that Pt was present in the form of complexes well approximated as $(\equiv Si-O-Zn)_{4-6}Pt$. These species exhibit exceptionally high catalytic activity, selectivity, and stability for both propane dehydrogenation to propylene and *n*-butane dehydrogenation to butene and 1,3-butadiene.[46,47]

Here, we explore the application of this catalyst design approach for generating isolated bimetallic centers in a siliceous zeolite framework with the aim of developing Rh-containing bimetallic centers for ethene hydroformylation. Both ≡SiOZnOH and ≡SiOCoOH Lewis acid sites produced in dealuminated zeolite Beta (DeAlBEA) were used to anchor isolated Rh atoms. These catalysts, designated as *x*Rh*y*Zn/Co-DeAlBEA (*x* and *y* are atomic ratios of an element with respect to the original inventory of Al), were characterized by infrared (IR) spectroscopy and XAS and investigated for ethene hydroformylation. Each catalyst was found to exhibit an activity and propanal selectivity greater than those reported for RhZn- and RhCo-containing hydroformylation catalysts prepared by other means. Our data show that ethene hydroformylation on both RhZn-DeAlBEA and RhCo-DeAlBEA proceeds via intermediates that were revealed by *in situ* IR spectroscopy carried out with $^{12}CO/^{13}CO$-C_2H_4-H_2 mixtures. It is proposed that the rate of hydroformylation is limited by a combination of generation and hydrogenation of acyl species, with the first of these steps being more nearly rate-limiting on RhZn-DeAlBEA and the second being more nearly rate-limiting on RhCo-DeAlBEA. The data suggest that ethane formation on each catalyst mainly occurs on Rh nanoparticles.

RESULTS

Creation of ≡SiOZn−OH and ≡SiOCo−OH Lewis Acid Sites in Silanol Nests of DeAlBEA. Aluminum atoms in HBEA zeolite, including both framework and extra-

https://doi.org/10.1021/jacs.2c11075
J. Am. Chem. Soc. 2023, 145, 2911−2929

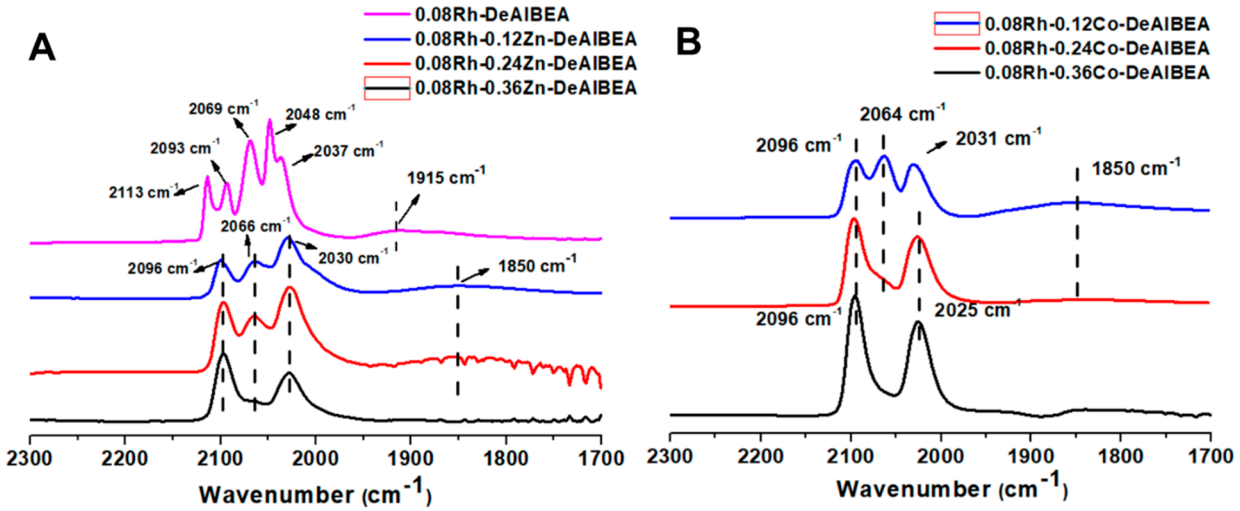

Figure 2. (A) CO probe molecule IR spectra of 0.08Rh-DeAlBEA and 0.08Rh-*x*Zn-DeAlBEA and (B) CO probe molecule IR spectra of 0.08Rh-*x*Co-DeAlBEA. In each case, the sample was first reduced in 10% H_2 at 473 K for 60 min, after which it was cooled in He to 303 K and exposed to 3 kPa of CO in He.

framework aluminum, were removed by dealumination, whereas the zeolite structure was preserved.[46] Silanol nests, consisting of hydrogen-bonded ≡Si−OH groups created by dealumination, were observed by the appearance of IR bands at 3550 and 3730 cm^{-1} (Figure 1A). Additional evidence of the formation of silanol nests was obtained from an IR spectrum of pyridine adsorbed on DeAlBEA. As shown in Figure 1B, two bands appeared, at 1592 and 1445 cm^{-1}, which are characteristic of pyridine interacting with hydrogen atoms of the ≡Si−OH groups in the silanol nests.[46,48,49] Zn and Co Lewis acid centers were created by grafting Zn or Co onto the ≡Si−OH groups in the silanol nests.[34,37,46] Detailed characterization of Zn-DeAlBEA is presented elsewhere.[46]

For direct comparison, we synthesized Co-DeAlBEA with a Co/Al ratio matching the Zn/Al ratio. ICP analysis (Table S2) indicates quantitative introduction of Co. The X-ray diffraction (XRD) pattern (Figure S1) and BET surface area of Co-DeAlBEA (Table S1) show that the zeolite structure was retained after introduction of Co and that no X-ray observable CoO_x nanoparticles formed, consistent with what we observed for Zn-DeAlBEA. IR spectra show that both silanol nests and internal silanol groups were consumed after introduction of Co, suggesting the generation of ≡SiOCoOH and ≡SiOCoOSi≡ species. With the introduction of Co, the intensity of the bands characterizing pyridine hydrogen-bonded to silanol nests (1592 and 1445 cm^{-1}) decreased (Figure 1B). Two new IR features were also observed, at 1608 and 1448 cm^{-1}, which are assigned to pyridine interacting with Co Lewis acid sites (Figure 1B and C). The intensities of these bands increased as the Co/Al ratio increased from 0.12 to 0.36. Relative to pyridine, 2,6-di-*tert*-butylpyridine (DTBPy) is sufficiently basic for proton transfer to occur from the weakly acidic OH groups associated with M−OH (M = Zn or Co) groups.[50,51] Adsorption of DTBPy on 0.36Co-DeAlBEA and on DeAlBEA resulted in the appearance of an IR band at 3356 cm^{-1} for 0.36Co-DeAlBEA (Figure S2), demonstrating that the grafted Co atoms were present as ≡SiOCo−OH groups. These findings parallel what we reported earlier for zinc centers in 0.36Zn-DeAlBEA, which demonstrated the presence of nests of weakly interacting ≡SiOZn−OH groups.[46,52]

Characterization of Rh Atoms Dispersed on DeAlBEA, Zn-DeAlBEA, and Co-DeAlBEA. Rh atoms were introduced onto Zn- and Co-DeAlBEA prepared with M/Al ratios of 0−0.36. ICP analysis (Table S2) showed near-quantitative incorporation of Rh in both cases. XRD (Figure S1) and BET data (Table S1) indicate that the zeolite framework structure was retained and that there were no obvious changes in the surface area or pore volume after introduction of Rh.

Figure 2 shows the IR spectra of CO adsorbed on DeAlBEA-, *x*Zn-DeAlBEA-, and *x*Co-DeAlBEA-supported Rh. These spectra were acquired with the aim of distinguishing between isolated Rh atoms and Rh nanoparticles. Table S3 is a summary of the assignments of ν_{CO} IR bands previously reported for Rh complexes and supported Rh; these data form the basis for assigning the features characterizing adsorbed CO observed in this investigation.[2,35,37]

IR spectra of CO adsorbed on 0.08Rh-DeAlBEA and 0.08Rh-*x*Zn-DeAlBEA acquired at 303 K are presented in Figure 2A. The 0.08Rh-DeAlBEA spectrum exhibits peaks at 2069 and 1915 cm^{-1} characteristic of linear and bridge-bonded CO, indicative of Rh clusters, and two sets of bands, centered at 2037 and 2048 cm^{-1}, and 2093 and 2113 cm^{-1}, associated with the symmetric and asymmetric stretches of rhodium *gem*-dicarbonyls. Considering the existence of various silanol groups on the surface of DeAlBEA, the observation of two sets of spectra characterizing rhodium *gem*-dicarbonyls is not surprising; they are attributed to isolated Rh atoms located in different local environments. For CO adsorbed on 0.08Rh-*x*Zn-DeAlBEA (x = 0.12−0.36) the spectra in Figure 2A exhibit only one set of bands, centered at 2030 and 2096 cm^{-1}. These features are identical to the symmetric and asymmetric stretches of rhodium *gem*-dicarbonyl species. For CO adsorbed on 0.08Rh-0.12Zn-DeAlBEA, both the bridge-bonded CO stretching band at 1850 cm^{-1} and that of the linearly adsorbed CO at 2066 cm^{-1} decreased in intensity relative to what was observed for CO adsorbed on 0.08Rh-DeAlBEA. As the Zn/Al ratio increased to 0.24 and then to 0.36, the intensities of the signals at 1850 and 2066 cm^{-1} decreased monotonically, and a monotonic increase occurred in the intensity of the bands characterizing rhodium *gem*-dicarbonyls. Moreover, almost no signal could be observed at 1850 cm^{-1} in the spectrum of

https://doi.org/10.1021/jacs.2c11075
J. Am. Chem. Soc. 2023, 145, 2911−2929

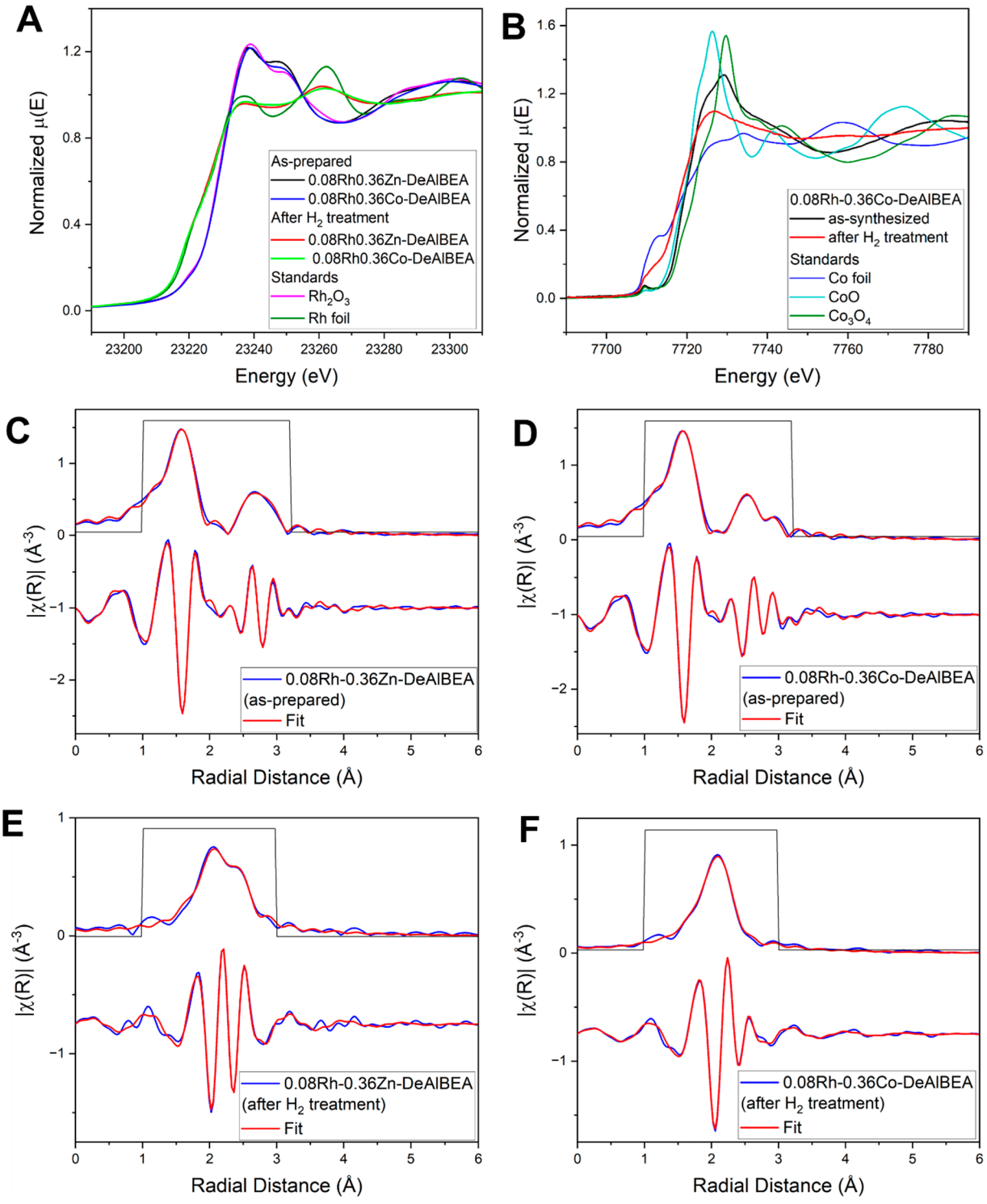

Figure 3. (A) Rh K-edge near-edge spectra of as-prepared and post-H_2-treatment 0.08Rh-0.36Zn-DeAlBEA and 0.08Rh-0.36Co-DeAlBEA and of standards characterizing Rh^0 (rhodium foil) and Rh^{3+} (Rh_2O_3); (B) Co K-edge near-edge spectra of 0.08Rh-0.36Co-DeAlBEA, as-prepared and after H_2 treatment at 473 K and of cobalt foil, CoO, and Co_3O_4 standards; (C−F) magnitude of Fourier transform and imaginary part of Rh K-edge EXAFS data and calculated fitting contribution (k^2-weighted) of the best fit of EXAFS data characterizing as-prepared 0.08Rh-0.36Zn-DeAlBEA, as-prepared 0.08Rh-0.36Co-DeAlBEA, post-H_2-treatment 0.08Rh-0.36Zn-DeAlBEA, and post-H_2-treatment 0.08Rh-0.36Co-DeAlBEA, respectively. Data were collected at 298 K. The range in k was 3.8−13.7 $Å^{-1}$ for the as-prepared samples and 3.6−13.2 $Å^{-1}$ for samples after H_2 treatment. The fit range in R was 1.0−3.2 Å for the as-prepared samples and 1.0−3.0 Å for samples after H_2 treatment. Details of fit parameters are presented in Table 1.

0.08Rh-0.36Zn-DeAlBEA, suggesting the absence of bridge-bound CO, which would be expected for Rh nanoparticles. However, the presence of the feature at 2066 cm^{-1} characteristic of linear-bound CO indicates a non-negligible presence of small Rh clusters.

https://doi.org/10.1021/jacs.2c11075
J. Am. Chem. Soc. 2023, 145, 2911−2929

Table 1. Fit Parameters Determined from EXAFS Data Acquired at Rh K-Edge for 0.08Rh-0.36Zn-DeAlBEA and 0.08Rh-0.36Zn-DeAlBEA, as-Synthesized and after H_2 Treatment[a]

Sample	Scattering path	Coordination number	ΔE_0, eV	R, Å	σ^2, Å^2	R-Factor	Reduced χ^2
As-prepared 0.08Rh-0.36Zn-DeAlBEA	Rh−O	6.6 ± 1.2	−1.9 ± 1.3	2.04 ± 0.007	0.0032 ± 0.0007	0.007	511
	Rh−O−Zn	0.7 ± 0.6		2.97 ± 0.045	0.0056 ± 0.0015[b]		
	Rh−O−Rh	3.6 ± 1.1		3.07 ± 0.010			
As-prepared 0.08Rh-0.36Co-DeAlBEA	Rh−O	6.5 ± 0.4	−1.77 ± 1.1	2.04 ± 0.005	0.0031 ± 0.0006	0.005	1067
	Rh−O−Co	2.3 ± 0.5		2.97 ± 0.011	0.0047 ± 0.0013[c]		
	Rh−O−Rh	2.4 ± 0.7		3.03 ± 0.009			
Reduced 0.08Rh-0.36Zn-DeAlBEA	Rh−Zn	3.5 ± 0.3	8 ± 0.9	2.54 ± 0.006	0.0091 ± 0.0006[d]	0.011	97
	Rh−Rh	4.2 ± 0.4		2.63 ± 0.007			
Reduced 0.08Rh-0.36Co-DeAlBEA	Rh−Co, Rh−Rh	4.9 ± 0.3	1.5 ± 1.0	2.57 ± 0.007	0.0110 ± 0.0009[e]	0.006	231
		3.0 ± 0.4		2.66 ± 0.008			

[a]Notation: R, scattering path length between the absorber and scattering atom; σ^2, mean square relative displacement; ΔE_0, inner potential correction. The R-factor is a measure of how closely the fit resembles the data. The reduced χ^2 is a statistical fitting metric normalized by the degrees of freedom. [b]σ^2 for Rh−(O)−Zn and Rh−(O)−Rh scattering paths were constrained to be equal. [c]σ^2 for Rh−(O)−Co and Rh−(O)−Rh scattering paths were constrained to be equal. [d]σ^2 for Rh−Zn and Rh−Rh scattering paths were constrained to be equal. [e]σ^2 for Rh−Co and Rh−Rh scattering paths were constrained to be equal.

IR spectra of CO adsorbed on 0.08Rh-xCo-DeAlBEA (x = 0.12−0.36) are shown in Figure 2B. The spectrum of 0.08Rh-0.12Co-DeAlBEA shows that the intensities of the bands characterizing bridging and linearly bonded CO (located at 1850 and 2064 cm^{-1}, respectively) were much weaker than those for the sample without Co, 0.08Rh-DeAlBEA. As the Co/Al ratio increased to 0.24, the intensities of the signals at 1850 and 2064 cm^{-1} decreased, and for Co/Al = 0.36, only a very weak band was observed, at 2064 cm^{-1} and practically no band intensity at 1850 cm^{-1}. Concurrently, the intensities of the rhodium *gem*-dicarbonyl bands, at 2096 and 2025−2031 cm^{-1}, increased as the Co/Al ratio increased from 0.12 to 0.36, in a manner similar to that observed for Rh-Zn-DeAlBEA.

In summary, the data show that both Zn-DeAlBEA and Co-DeAlBEA are more effective in dispersing Rh than DeAlBEA itself and that, as the Zn/Al or Co/Al ratio increases for a constant Rh loading, more of the Rh is dispersed atomically, as indicated by the increased intensity of IR bands for *gem*-dicarbonyl species relative to those for linear- and bridge-bonded CO. We also find that for a given M/Al ratio Co is more effective than Zn in dispersing Rh.

Additional information about the oxidation state and coordination environment of Rh in as-prepared 0.08Rh-0.36Zn-DeAlBEA and 0.08Rh-0.36Co-DeAlBEA was obtained from XAS data recorded at the Rh K-edge. The near-edge spectra of both as-synthesized samples are characterized by edge energies and white line intensities similar to those of Rh^{3+} in Rh_2O_3 (Figure 3A).[53] The Fourier transforms of the Rh K-edge extended X-ray absorption fine structure (EXAFS) spectra of the as-synthesized samples are fitted satisfactorily with a Rh−O scattering path (at a radial distance ca. 2.0 Å), a Rh−O−Co (Zn) scattering path, and a Rh−O−Rh scattering path (at a distance ca. 2.95−3.1 Å) (Table 1, Figure 3C,D, and Figures S3 and S4). Fitting of the EXAFS spectra indicate that Rh was coordinated, on average, to 6 O atoms in the first coordination shell. The EXAFS spectrum characterizing 0.08Rh-0.36Co-DeAlBEA could not be fitted satisfactorily with a model consisting of only Rh−O−Rh paths; an additional Rh−O−Co path was necessary to fit the data satisfactorily, providing evidence of the interaction of Rh with Co (Figure S3, Table S4). The 0.08Rh-0.36Zn-DeAlBEA EXAFS data, on the other hand, were satisfactorily fitted with a model including only Rh−O and Rh−O−Rh scattering paths, and the addition of a Rh−O−Zn path only marginally improved the goodness of fit (Figure S4, Table S4). The ratio of the calculated Rh−O−Co coordination number to the Rh−O−Rh coordination number for 0.08Rh-0.36Co-DeAlBEA is much higher than the ratio of the Rh−O−Zn coordination number to the Rh−O−Rh coordination number for 0.08Rh-0.36Zn-DeAlBEA, suggesting that Rh was dispersed as a consequence of the stronger interactions with Co than with Zn in the as-prepared samples. We emphasize that EXAFS data do not establish unique structures but instead represent mixtures of structures, as expected for samples such as ours and confirmed by the full width at half-maximum values of the IR bands for adsorbed CO (Figure 2), which are wider than those in spectra of more nearly uniform samples.[54,55]

Treatment of the samples in 10% H_2 in He at 473 K resulted in marked changes in the Rh K-edge XANES and EXAFS data. Figure 3A shows that the white line decreased in intensity after H_2 treatment, and the absorption edge shifted to lower energy, indicating a reduction of the Rh in each sample. Comparison of the near-edge spectra of the treated samples with that of a Rh foil standard implies that the Rh was essentially metallic after the treatment.

The analysis of the EXAFS data for H_2-treated samples (Figure 3E,F, Table 1) did not include contributions from Rh−O scattering paths. The fits of the Fourier-transformed EXAFS patterns provide evidence of Rh coordination with both Rh and Co (or Zn) atoms. Attempts to fit the EXAFS data with only Rh−Rh coordination or only Rh−Co (or Rh−Zn) coordination gave unsatisfactory fits (Figures S5 and S6, Table S4). The fitting results also indicate that the ratio of coordination numbers of Rh−Co:Rh−Rh scattering paths in 0.08Rh-0.36Co-DeAlBEA (1.63 ± 0.1) is higher than the ratio of coordination numbers of Rh−Zn:Rh−Rh scattering paths in 0.08Rh-0.36Zn-DeAlBEA (0.83 ± 0.1), suggesting that Rh is more highly dispersed when the second metal is Co rather than Zn. These findings are consistent with the IR spectra of CO adsorbed on the reduced 0.08Rh-0.36Co-DeAlBEA and 0.08Rh-0.36Zn-DeAlBEA, which indicate a higher fraction of isolated Rh atoms (inferred to be present as rhodium *gem*-dicarbonyls) on 0.08Rh-0.36Co-DeAlBEA.

The state of cobalt in the as-synthesized and H_2-treated 0.08Rh-0.36Co-DeAlBEA was probed by X-ray absorption near-edge structure (XANES) at the Co K-edge. The spectrum

https://doi.org/10.1021/jacs.2c11075
J. Am. Chem. Soc. 2023, 145, 2911−2929

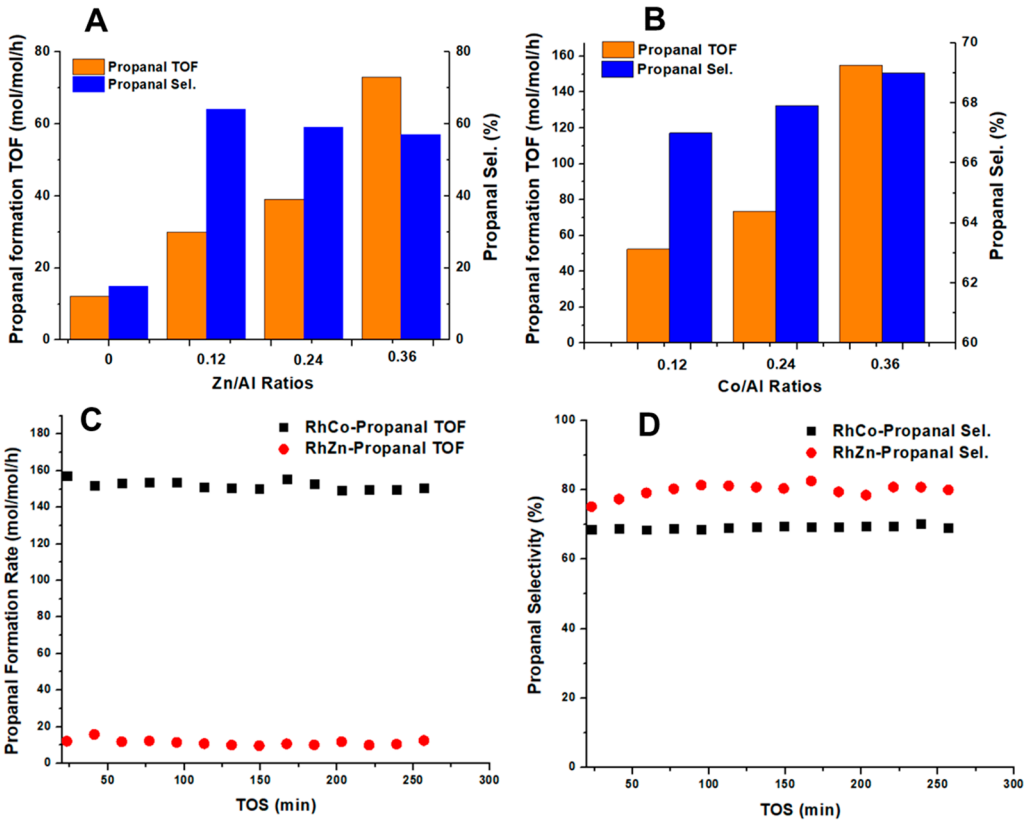

Figure 4. (A) Ethene hydroformylation activity and propanal selectivity in reaction catalyzed by 0.08Rh-DeAlBEA and 0.08Rh-*x*Zn-DeAlBEA with various Zn loadings; (B) ethene hydroformylation activity and propanal selectivity in reaction catalyzed by 0.08Rh-*x*Co-DeAlBEA with various Co loadings; (C) comparison of ethene hydroformylation activities characterizing 0.08Rh-0.36Zn-DeAlBEA and 0.08Rh-0.36Co-DeAlBEA; (D) comparison of propanal selectivities characterizing 0.08Rh-0.36Zn-DeAlBEA and 0.08Rh-0.36Co-DeAlBEA. Reaction conditions: (A) Mass of catalyst, 20 mg; temperature *T*, 443 K; total feed flow rate, 30 mL(NTP)/min; partial pressures P_{C2H4}, 33.8 kPa; P_{CO}, 33.8 kPa; P_{H2}, 33.8 kPa. (B) Mass of catalyst, 20 mg; *T*, 403 K; total feed flow rate, 90 mL(NTP)/min; P_{C2H4}, = 33.8 kPa; P_{CO}, 33.8 kPa; P_{H2}, 11.3 kPa, balance, helium; total pressure was atmospheric. (C, D) Mass of catalyst, 20 mg; *T*, 403 K; total feed flow rate, 90 mL(NTP)/min; P_{C2H4}, 33.8 kPa; P_{CO}, 33.8 kPa; P_{H2}, 11.3 kPa, balance, He; total pressure was atmospheric. TOS is time on stream in the flow reactor. TOFs shown in panels (A) and (B) are based on total number of Rh atoms in the catalyst sample.

of the as-synthesized 0.08Rh-0.36Co-DeAlBEA (Figure 3B) is characterized by a prominent white line and an edge energy similar to that of Co^{2+} in the standard CoO, indicating positively charged cobalt. Attempts to fit the XANES data representing the as-synthesized 0.08Rh-0.36Co-DeAlBEA by a linear combination fitting (LCF) of CoO, Co_3O_4, and Co foil standards yielded a suboptimal fit, with significant deviations from the data (Figure S7). This result suggests that the local coordination environment of Co was different from those of the bulk oxide standards. The LCF fit indicates that Co was completely oxidized, with the data being best fitted by a linear combination of CoO and Co_3O_4 spectra, weighted equally. Treatment of the sample in H_2 at 473 K resulted in partial reduction of Co, which is evident from the lowering of the white line intensity and edge energy (Figure 3B). Therefore, Co is inferred to have been present as a mixture of metallic and oxidized species in the sample after H_2 treatment.

Ethene Hydroformylation and Hydrogenation Catalyzed by Rh-Zn-DeAlBEA and Rh-Co-DeAlBEA. Ethene hydroformylation catalyzed by 0.08Rh-*x*Zn-DeAlBEA (*x* = 0−0.36) was investigated to determine the influence of Zn loading on the catalytic activity and selectivity for a fixed set of reaction conditions (*T* = 443 K, P_{C2H4} = 33.8 kPa, P_{CO} = 33.8 kPa, P_{H2} = 33.8 kPa, 101 kPa total pressure). The only products observed were ethane and propanal. Zn-DeAlBEA and DeAlBEA showed no measurable hydroformylation activity under our conditions. As shown in Figure 4A, the TOF characterizing 0.08Rh-DeAlBEA was 12 h^{-1}, but the propanal selectivity was only 15%. When the Zn/Al ratio increased from 0.12 to 0.36, the propanal TOF increased from 30 to 73 h^{-1}; the propanal selectivity increased to 64% but then decreased slightly to 57% as the Zn/Al ratio increased to 0.36. The continuous increase in the propanal TOF with increasing Zn/Al ratio is consistent with the increased dispersion of Rh made evident by the CO IR spectra. The slight decrease in propanal selectivity for 0.08Rh-0.36Zn-DeAlBEA compared with 0.08Rh-0.12Zn-DeAlBEA is attributed to the weak hydrogenation activity of Zn Lewis acid centers, consistent with reports for Zn-SiO_2.[56]

Ethene hydroformylation was also investigated for 0.08Rh-*x*Co-DeAlBEA (*x* = 0.12−0.36) under the same reaction conditions. The only products observed were ethane and propanal. Co-DeAlBEA showed no measurable hydroformylation activity. The propanal TOF characterizing 0.08Rh-0.12Co-DeAlBEA was 52 h^{-1}, and the selectivity was 67% (Figure 4B). As the Co/Al ratio increased to 0.24 and then to 0.36, the propanal TOF increased to 73 h^{-1} and then to 155 h^{-1}, and the propanal selectivity increased slightly to 68 and then to 69%. The continuous increase in propanal formation

https://doi.org/10.1021/jacs.2c11075
J. Am. Chem. Soc. 2023, 145, 2911−2929

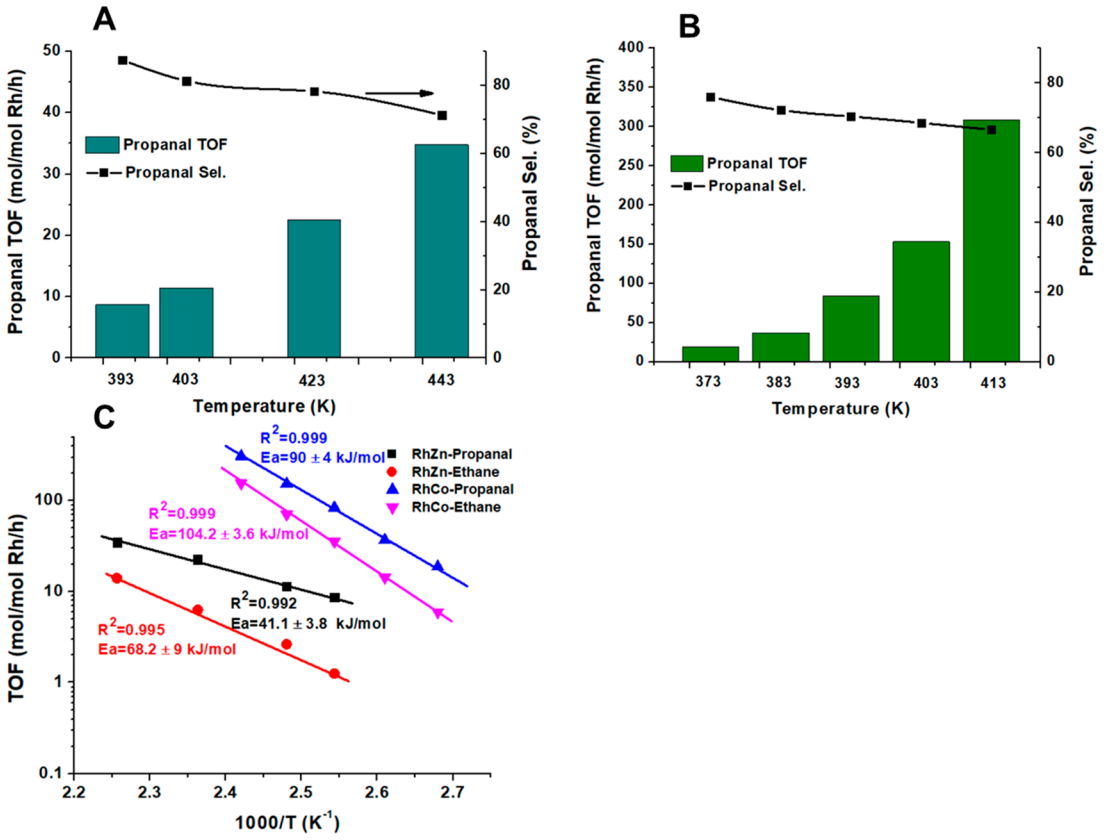

Figure 5. (A) Influence of temperature on ethene hydroformylation activity and propanal selectivity catalyzed by 0.08Rh-0.36Zn-DeAlBEA; (B) influence of temperature on ethene hydroformylation activity and propanal selectivity catalyzed by 0.08Rh-0.36Co-DeAlBEA; (C) Arrhenius plots for propanal formation and ethane formation catalyzed by 0.08Rh-0.36Zn-DeAlBEA and 0.08Rh-0.36Co-DeAlBEA. Reaction conditions: (A) mass of catalyst, 20 mg; total feed flow rate, 90 mL(NTP)/min; P_{C2H4}, 33.8 kPa; P_{CO}, 33.8 kPa; P_{H2}, 11.3 kPa, balance He; total pressure was atmospheric.

rate is consistent with the increased dispersion of Rh atoms observed by the CO IR spectra (Figure 2).

A direct comparison of the performances of 0.08Rh-0.36Zn-DeAlBEA and 0.08Rh-0.36Co-DeAlBEA was made under the following reaction conditions: T = 403 K, P_{C2H4} = 33.8 kPa, P_{CO} = 33.8 kPa, P_{H2} = 11.3 kPa, balance, He; total pressure = 101 kPa. As shown in Figure 4C, 0.08Rh-0.36Zn-DeAlBEA exhibited a propanal TOF of 10 h^{-1}, whereas that for 0.08Rh-0.36Co-DeAlBEA was 155 h^{-1}. On the other hand, the propanal selectivity of 0.08Rh-0.36Zn-DeAlBEA (80%) was higher than that of 0.08Rh-0.36Co-DeAlBEA (68%) (Figure 4D). Considering the similar Rh dispersions of 0.08Rh-0.36Zn-DeAlBEA and 0.08Rh-0.36Co-DeAlBEA, the 15.5-fold higher hydroformylation activity of 0.08Rh-0.36Co-DeAlBEA is attributed to differences in the electronic effects of Co vs Zn on Rh, as discussed below.

Data showing the influence of temperature on ethene hydroformylation catalysis for both 0.08Rh-0.36Zn-DeAlBEA and 0.08Rh-0.36Co-DeAlBEA are presented in Figure 5. Lowering the temperature enhanced the selectivity to propanal for both catalysts. This pattern is consistent with the higher apparent activation energy for ethene hydrogenation than that for hydroformylation (Figure 5C). Specifically, for 0.08Rh-0.36Zn-DeAlBEA, as the temperature increased from 393 K to 443 K, the propanal selectivity decreased from 87% to 71%. And for 0.08Rh-0.36Co-DeAlBEA, as the temperature increased from 373 K to 413 K, the propanal selectivity decreased from 76% to 67%. Within the same temperature range, the propanal activity was always higher and the propanal selectivity lower for 0.08Rh-0.36Co-DeAlBEA than for 0.08Rh-0.36Zn-DeAlBEA. The apparent activation energies for hydroformylation and hydrogenation catalyzed by 0.08Rh-0.36Zn-DeAlBEA are 41 and 68 kJ/mol, respectively (Figure 5C), and the corresponding values characterizing 0.08Rh-0.36Co-DeAlBEA are 90 and 104 kJ/mol, respectively.

The apparent activation energies for propanal formation reported here can be compared with those reported for Rh/SiO_2 (42−72 kJ/mol),[35,38,57] Zn/Rh/SiO_2 (59 kJ/mol),[38] Rh/Y zeolite (39−56 kJ/mol),[57,58] Rh/NaY zeolite (27 kJ/mol),[59] Rh/Al_2O_3 (43−48 kJ/mol),[28,57] Rh-ReO_x/Al_2O_3 (46−49 kJ/mol),[28] RhCo/SiO_2 (38 kJ/mol),[35] and $RhCo_3$/MCM-41 (55 kJ/mol).[9] Compared with these values, the apparent activation energy for propanal formation on 0.08Rh-0.36Zn-DeAlBEA (41 kJ/mol) is similar; however, that for 0.08Rh-0.36Co-DeAlBEA (90 kJ/mol) is markedly higher.

Similarly, the apparent activation energies for ethane formation on the catalysts reported here can be compared with those reported for Rh/SiO_2 (60−121 kJ/mol),[35,38,57] Zn/Rh/SiO_2 (134−167 kJ/mol),[38] Rh/Y zeolite (72−90 kJ/mol),[57] Rh/NaY zeolite (90 kJ/mol),[59] Rh/Al_2O_3 (82−110 kJ/mol),[28,57] Rh-ReO_x/Al_2O_3 (102−109 kJ/mol),[28] RhCo/SiO_2 (74 kJ/mol),[35] and $RhCo_3$/MCM-41 (91 kJ/mol).[9] In this case, all of the apparent activation energies for ethane formation reported previously are similar to those for 0.08Rh-0.36Co-DeAlBEA (104 kJ/mol) and 0.08Rh-0.36Zn-DeAlBEA (90 kJ/mol).

https://doi.org/10.1021/jacs.2c11075
J. Am. Chem. Soc. 2023, 145, 2911−2929

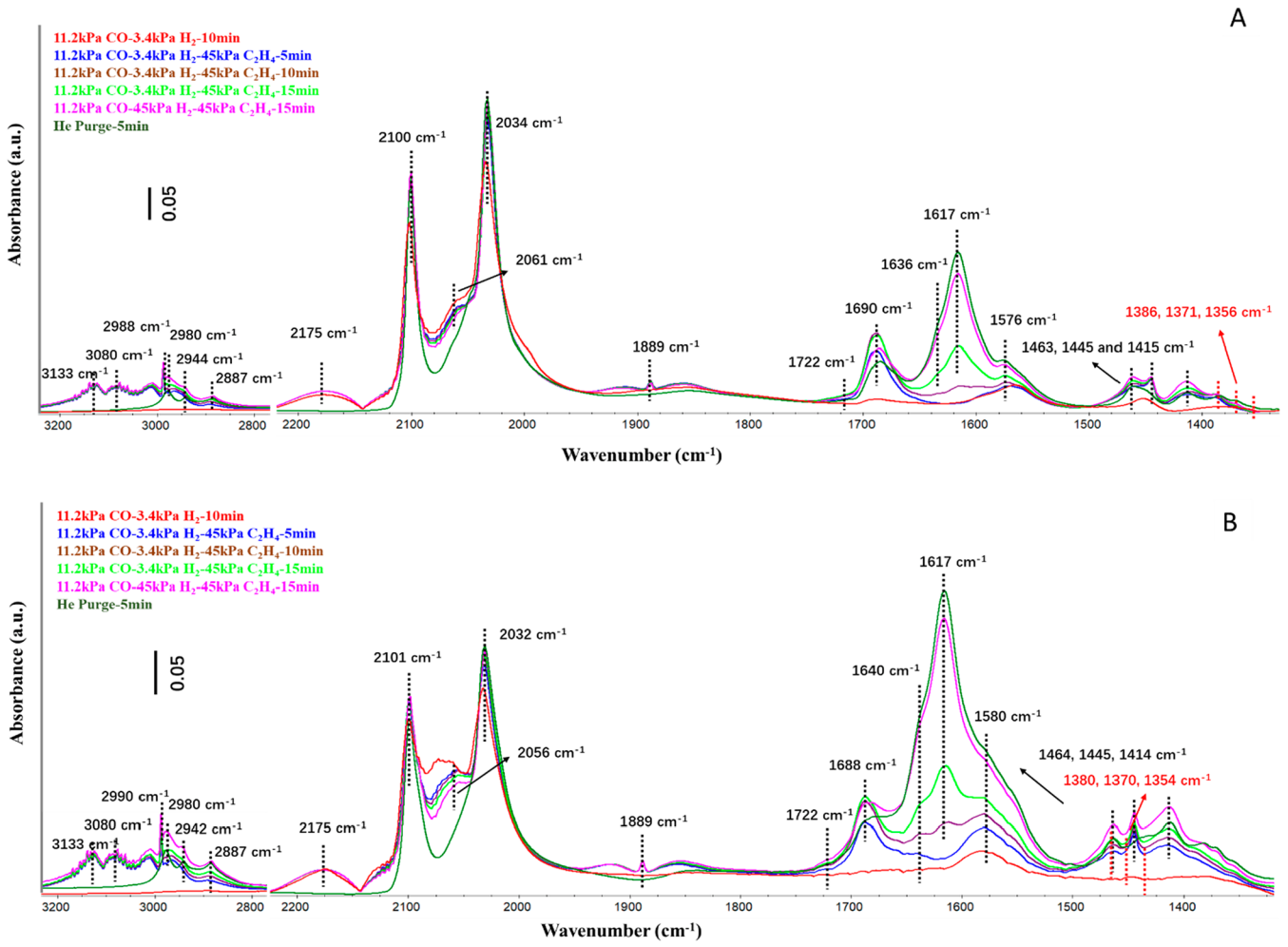

Figure 6. IR spectra acquired during ethene hydroformylation catalysis on 0.08Rh-0.36Zn-DeAlBEA (A) and 0.08Rh-0.36Co-DeAlBEA (B). Reaction conditions: 403 K, total flow rate = 10/40/40 mL(NTP) min^{-1}.

H/D Kinetic Isotope Effect. Hydroformylation experiments were carried out with both H_2 and D_2 to determine the kinetic isotope effects (KIE) characterizing the performance of 0.08Rh-0.36Co-DeAlBEA and 0.08Rh-0.36Zn-DeAlBEA. Results of rate experiments carried out at 403 K are shown in Figure S8. The initial feed to each catalyst was $CO/C_2H_4/H_2$/He = 30/30/10/20 mL(NTP) min^{-1}, and after 60 min on stream, the feed H_2 stream was switched to D_2 at the same rate; then, after an additional 60 min, the feed was switched back to that containing H_2.

The rates of ethene hydroformylation and hydrogenation characterizing each catalyst decreased when D_2 replaced H_2, and the effect was greater for the Co-containing catalyst. The KIE was calculated by averaging the rate of formation of each product with each hydrogen isotope to obtain the corresponding values of r_H and r_D. The KIE values (r_H/r_D) for hydroformylation and hydrogenation on 0.08Rh-0.36Zn-DeAlBEA were found to be 1.2 and 1.4, respectively, and 1.6 and 1.7, respectively, for reaction on 0.08Rh-0.36Co-DeAlBEA. The positive KIE values suggest the involvement of hydrogen in the rate-determining steps of each reaction, with the greater effect for 0.08Rh-0.36Co-DeAlBEA than for 0.08Rh-0.36Zn-DeAlBEA.

In situ IR spectra were acquired for both 0.08Rh-0.36Zn-DeAlBEA and 0.08Rh-0.36Co-DeAlBEA. Each catalyst pellet was first reduced in a 10% H_2 in He at 473 K for 1 h, and then the temperature was reduced to 403 K, after which H_2 was replaced by the hydroformylation reaction feed mixture. In these experiments, the partial pressures of CO and C_2H_4 were 11.2 and 45 kPa, respectively, and the partial pressure of H_2 was kept at 3.4 or 45 kPa with the balance of the feed stream being He. The total gas flow rate was 90 mL(NTP)/min. The results are presented in Figure 6A and B.

The spectrum of CO adsorbed on 0.08Rh-0.36Zn-DeAlBEA from a mixture containing 11.2 kPa of CO and 3.4 kPa of H_2 (Figure 6A) includes bands at 2100 and 2034 cm^{-1}, corresponding to the symmetric and asymmetric C−O stretching vibrations, respectively, of CO on positively charged Rh in rhodium *gem*-dicarbonyls.[60−62] The spectrum also includes a band centered at ∼2061 cm^{-1} corresponding to CO linearly adsorbed on Rh^0 atoms and a broad signal at 2175 cm^{-1} for gas-phase CO.[60−62] As discussed below, the linearly adsorbed CO was weakly bound and readily removed when the IR cell was purged with He.

Upon addition of 45 kPa of C_2H_4 to the CO/H_2 mixture, bands associated with the rotations and vibrations of gas-phase ethene were observed at ∼1445, ∼1920−1820, and ∼3200−2990 cm^{-1}.[63] Moreover, bands appeared at 1356, 1371, 1386, 1415, and 1463 cm^{-1}, characteristic of symmetric and asymmetric C−H bending vibrations of CH_2 and CH_3 groups in ethyl or acyl species. Such features have been observed at ∼1470−1360 cm^{-1} for ethene interacting with Brønsted acidic

https://doi.org/10.1021/jacs.2c11075
J. Am. Chem. Soc. 2023, 145, 2911−2929

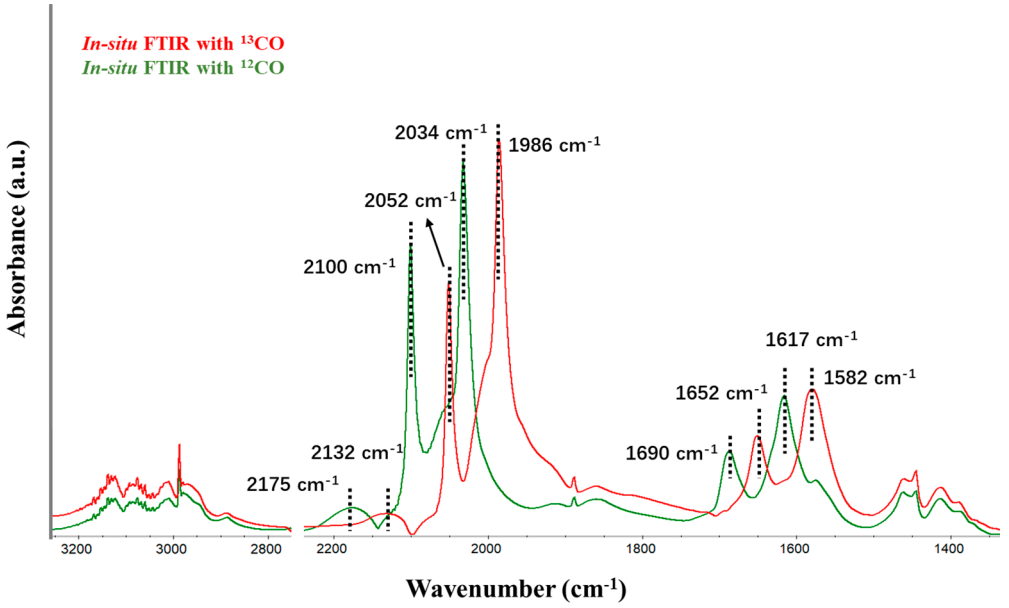

Figure 7. Comparison of IR spectra acquired during ethene hydroformylation catalysis on 0.08Rh-0.36Zn-DeAlBEA with ^{12}CO and ^{13}CO reactants. Reaction conditions: 403 K, ($^{12}CO/^{13}CO$)/C_2H_4/H_2 = 10/40/40 mL(NTP) min^{-1}.

OH groups in zeolites.[64,65] The observation of symmetric and asymmetric C−H stretching vibrations in the range of ∼3000−2800 cm^{-1} provides further evidence of the formation of rhodium alkyl or acyl complexes.[9] The bands located between 1463 and 1415 cm^{-1} might also be assigned to C−H bending vibrations of C_2H_4 π-bonded to Rh centers. Organorhodium complexes containing π-bonded C_2H_4 ligands exhibit a band at 1440−1419 cm^{-1} assigned to C−H bending vibrations of CH_2 groups ($\delta(CH_2)$) and a band at 1516−1480 cm^{-1} that includes contributions from C═C stretching vibrations ($\nu_{C=C}$) and C−H bending vibrations of CH_2 groups.[66] And π-bonded C_2H_4 ligands in zeolite-supported Rh(CO)(C_2H_4) complexes exhibit bands at 1438 ($\delta(CH_2)$) and 1536 cm^{-1} ($\delta(CH_2)$ + $\nu_{C=C}$).[63] Because bands at 1516−1480 cm^{-1} ascribed to $\delta(CH_2)$ + ν(C═C) were not observed after exposure of the sample to C_2H_4, it is not likely that the bands at 1464−1414 cm^{-1} (Figure 6A) arise from C−H bending vibrations of C_2H_4 π-bonded to Rh centers.

As the reaction proceeded, there was a gradual increase in the intensity of the bands at 3000−2800 and 1500−1350 cm^{-1} (Figure 6A), and new features appeared in the range of 1750−1500 cm^{-1}, which are assigned to C═O stretching vibrations of adsorbed acyl species, presumably propionyl ($CH_3CH_2CO^*$).[67−70] It has been reported that acyl groups in various Rh complexes exhibit C═O stretching vibrations at 1705−1635 cm^{-1}.[71−73] Support for these assignments can be drawn from the observation of acyl species exhibiting bands at 1695, 1673, and 1645 cm^{-1} during ethene hydroformylation catalyzed by $RhH(CO)L_3$ (L = $P(3,5\text{-}(CF_3)_2(C_6H_3)_3$) in supercritical CO_2.[67]

IR spectra acquired during hydroformylation catalyzed by 0.08Rh-0.36Co-DeAlBEA (Figure 6B) show that prior to the introduction of C_2H_4 to a mixture of CO and H_2, the only features observed are those for CO stretching bands of gas-phase and adsorbed CO. These features include bands at 2101 and 2032 cm^{-1}, characterizing symmetric and asymmetric C−O stretching vibrations of rhodium *gem*-dicarbonyls (Table S3), a band at ∼2056 cm^{-1} assigned to linearly adsorbed CO on Rh^0 atoms, and a broad signal at 2175 cm^{-1} assigned to gas-phase CO.[60−62] Upon addition of 45 kPa C_2H_4 to the CO/H_2 mixture, bands associated with the rotations and vibrations of gas-phase ethene appeared at ∼1445, ∼1920−1820, and ∼3200−2990 cm^{-1}.[63] Bands were also evident at 1354, 1370, 1380, 1414, and 1464 cm^{-1}, assigned to symmetric and asymmetric C−H bending vibrations of CH_2 and CH_3 groups and bands at ∼3000−2800 cm^{-1} assigned to symmetric and asymmetric C−H stretching vibrations. These features are similar to those observed for 0.08Rh-0.36Zn-DeAlBEA and are assigned to Rh alkyl or Rh acyl complexes.[9] In line with what was observed for 0.08Rh-0.36Zn-DeAlBEA, changes were also seen in the range of 1750−1500 cm^{-1}, which provide evidence for C═O vibrations associated with acyl ligands.

As the catalytic reaction progressed, gradual increases were observed in intensity of the bands at 3000−2800, 1750−1500, and 1500−1350 cm^{-1}, indicating the formation and accumulation of intermediates associated with ethene hydroformylation. The spectra presented in Figure 6A and B include features suggesting the formation of acyl groups (i.e., the bands appearing in the range of 1750−1500, 2800−3000, and 1400−1500 cm^{-1}). To confirm this assignment, IR spectra were obtained with ^{13}CO in the reaction mixture and compared with those recorded with ^{12}CO. Figure 7 shows that when ^{12}CO was replaced with ^{13}CO, the CO bands for rhodium *gem*-dicarbonyls shifted to 2052 and 1986 cm^{-1}, with that characterizing linearly adsorbed CO on Rh^0 atoms shifting to ∼2013 cm^{-1} and that characterizing gas-phase CO shifting to 2134 cm^{-1}. More importantly, the bands at 1700−1600 cm^{-1} corresponding to ^{12}CO-containing intermediates of the hydroformylation shifted to 1652−1582 cm^{-1}, as expected for ^{13}CO-containing acyl ligands.

Therefore, we conclude that, for both catalysts, the IR signals observed at 1700−1600 cm^{-1} can be assigned to hydroformylation reaction intermediates generated from adsorbed ethyl groups and CO. In support of this assignment, we emphasize that the IR spectrum of propanal adsorbed at 403 K on Rh-Co-DeAlBEA (Figure S9) exhibits a band at 1617 cm^{-1}, attributable to the C═O stretch in propionyl. This feature is distinct from that observed at 1722 cm^{-1} for gas-

https://doi.org/10.1021/jacs.2c11075
J. Am. Chem. Soc. 2023, 145, 2911−2929

phase propanal, implying that, upon adsorption, propanal loses the aldehydic hydrogen atom to form an adsorbed propionyl group.

A separate IR experiment was carried out to further characterize these intermediates. Figure 8 shows spectra

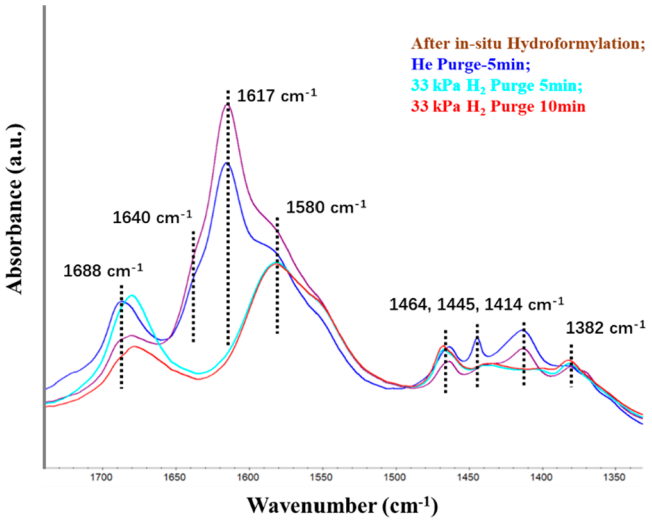

Figure 8. Influence of He and H_2 purges on IR spectra after ethene hydroformylation catalysis on 0.08Rh-0.36Co-DeAlBEA. Temperature: 403 K; feed composition: $CO/C_2H_4/H_2$ = 10/40/40 mL(NTP) min^{-1}; total gas flow rates of pure He and 33 kPa H_2 were 90 mL min^{-1}.

acquired upon termination of ethene hydroformylation, purging of the IR cell with He for 5 min, and further purging with H_2 at a partial pressure of 33 kPa. The band at 1617 cm^{-1} increased in intensity after the 5 min He purge, but the bands at 1640 and 1688 cm^{-1} decreased only slightly in intensity. However, when the purge gas was switched to H_2, the intensity of the 1617 cm^{-1} band decreased immediately, in the first 5 min. This change was accompanied by a gradual decline in the intensity of the 1688 cm^{-1} band.

We propose that the band at 1688 cm^{-1} represents coadsorbed ethyl and carbonyl groups in a cyclic acyl precursor involving agostic bonding of methylene H atoms in the ethyl group, as illustrated in Scheme 1. Evidence for such a structure is provided by the theoretical work of Derecskei-Kovacs and Marynick,[74] who showed that methyl migration to coordinated CO in the reaction $Mn(CO)_5CH_3 + CO \rightarrow Mn(CO)_5(C(O)CH_3)$ occurs primarily via initial formation of an agostic acyl complex for which the activation barrier is very low and the barrier for the reverse reaction is negligible. Isomerization of the agostic acyl complex to give an acyl complex that is lower in energy than the agostic acyl complex involves the addition of a CO molecule to give the final product, $Mn(CO)_5[C(O)Me]$.

XAS of 0.08Rh-0.36Co-DeAlBEA Acquired during Ethene Hydroformylation Catalysis. Rh K-edge XAS data of 0.08Rh-0.36Co-DeAlBEA collected during ethene hydroformylation catalysis at 388 K (Figure 9, Figures S10 and S11) provide further confirmation of the Rh dicarbonyl formation deduced from *in situ* IR spectra. These XAS data also provide evidence of fragmentation and further dispersion of Rh clusters by corrosive chemisorption of CO under reaction conditions. In the XAS experiment, the sample was treated in 10% H_2 in He for 1 h at 473 K, and then ethene hydroformylation was conducted at 388 K with a feed composition of $H_2/CO/C_2H_4/He$ = 2.2/6.6/2.2/9.

The near-edge spectrum (Figure 9A) shows a small increase in the white line intensity when reduced 0.08Rh-0.36Co-DeAlBEA was exposed to the ethene hydroformylation feed, possibly indicating some degree of Rh oxidation. EXAFS spectra of 0.08Rh-0.36Co-DeAlBEA acquired during reaction at 388 K and after cooling to room temperature are satisfactorily represented with Rh−Co, Rh−Rh, and single and multiple Rh−C and Rh−C and Rh−O scattering paths (the last associated with CO molecules coordinated to Rh) (Table S5, Model #1, Figure 9B,C, Figure S11A−C). The Rh−Rh coordination number is lower for 0.08Rh-0.36Co-DeAlBEA under ethene hydroformylation conditions than that observed after reduction. We reemphasize that these spectra do not unequivocally determine a single structural model—spectra collected during the catalytic reaction can also be fitted with a similar goodness-of-fit (probed by the *R*-factor and reduced-χ^2 values) by a model (Table S5, Model #2, Figure S11D−F) consisting of only Rh−Co, Rh−C, and Rh−C and Rh−O paths (corresponding to adsorbed CO), without a Rh−Rh shell—and this latter model would point to Rh predominantly in an atomically dispersed state, coordinated with Co. The overlapping contributions of the Rh−Rh and Rh−C or Rh−O paths make it challenging to resolve the individual contributions and choose between the two models. These points reflect the nonuniformity of the samples and the limitations of EXAFS spectroscopy in resolving mixtures. Further details of the interpretation of the EXAFS data are given in the Supporting Information. It is significant that both models indicate a decrease in the Rh−Rh coordination number upon exposure of the sample to the reactants. This finding is in line with literature reports of the oxidative fragmentation of Rh clusters into single atoms (in rhodium *gem*-dicarbonyls) by CO, with possible involvement of support OH groups in the fragmentation chemistry.[75,76]

On the basis of the *in situ* XAS data and IR spectra of adsorbed CO, we infer that most of the Rh was atomically dispersed during ethene hydroformylation; however, the presence of a small fraction of Rh clusters cannot be ruled out. Both of the above-mentioned models used to fit the *in situ* EXAFS data indicate a Rh−C coordination number >1 (in the range of 1.4 to 2.0), consistent with the observation of rhodium dicarbonyl species by IR spectroscopy.

Kinetics of Ethene Hydroformylation and Hydrogenation. Rates of ethene hydroformylation and hydrogenation catalyzed by 0.08Rh-0.36Zn-DeAlBEA and 0.08Rh-0.36Co-DeAlBEA

Scheme 1. Simplified Structure Suggested for Acyl Precursor on a Rh Atom in the Catalyst

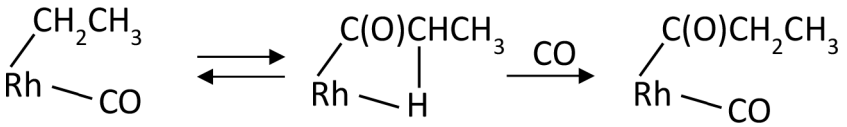

https://doi.org/10.1021/jacs.2c11075
J. Am. Chem. Soc. 2023, 145, 2911−2929

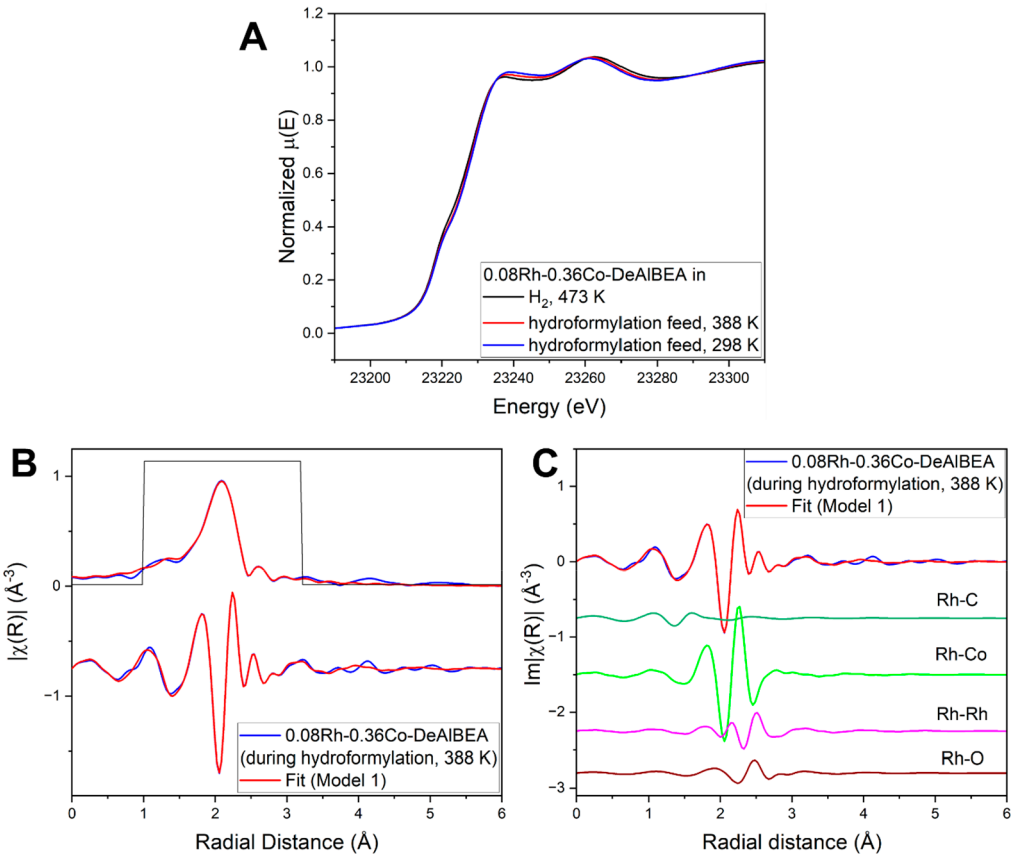

Figure 9. (A) Rh K-edge near-edge spectra of 0.08Rh-0.36Co-DeAlBEA after H_2 pretreatment and during ethene hydroformylation catalysis; reaction conditions: T = 388 K, pressure = 1 bar, feed composition = $H_2/CO/C_2H_4/He$ = 2.2/6.6/2.2/9, WHSV = 30 L h^{-1} g^{-1}; (B) magnitude of Fourier transform and imaginary part of Rh K-edge EXAFS data and calculated fitting contribution (k^2-weighted) of best fit of EXAFS modeling for 0.08Rh-0.36Co-DeAlBEA during ethene hydroformylation catalysis at 388 K; (C) imaginary part and calculated contributions of the Fourier transform of the data, Rh−C, Rh−Co, Rh−Rh, and Rh−(C)−O (k^2-weighted). Feed composition during reaction was $H_2/CO/C_2H_4/He$ = 2.2/6.6/2.2/9. The range in k was 3.7−13.4 Å^{-1}, and the range in R was 1.0−3.2 Å. Details of fits are presented in Table 2.

Table 2. Reaction Orders Characterizing Ethene Hydroformylation and Hydrogenation Catalyzed by 0.08Rh-0.36Co/Zn-DeAlBEA

Sample	Reactant	Hydroformylation reaction order	Hydrogenation reaction order	Apparent activation energy of hydroformylation reaction[a]/kJ mol^{-1}	Apparent activation energy of hydrogenation reaction[b]/kJ mol^{-1}
0.08Rh-0.36Zn-DeAlBEA	CO	−0.56 ± 0.04	−1.2 ± 0.02	41 ± 4	68 ± 9
	C_2H_4	0.85 ± 0.01	0.85 ± 0.03		
	H_2	0.67 ± 0.01	1.0 ± 0.0		
0.08Rh-0.36Co-DeAlBEA	CO	−0.81 ± 0.02	−1.10 ± 0.02	90 ± 4	104 ± 4
	C_2H_4	0.90 ± 0.02	0.90 ± 0.03		
	H_2	0.78 ± 0.01	1.0 ± 0.0		

[a]Apparent activation energies of hydroformylation from Figure 5C. [b]Apparent activation energies of hydrogenation from Figure 5C.

were measured at 403 K as a function of the CO, ethene, and H_2 partial pressures. Each partial pressure was varied individually, while the others were held constant, and the flow rate of He was adjusted to maintain a constant total flow rate of 90 mL(NTP) min^{-1}. The results (Figures S13 and S14) show that the reaction orders in CO, C_2H_4, and H_2 for propanal formation are −0.56, 0.85, and 0.67, respectively, for 0.08Rh-0.36Zn-DeAlBEA and −0.81, 0.90, and 0.78, respectively, for 0.08Rh-0.36Co-DeAlBEA. The corresponding reaction orders in CO, C_2H_4, and H_2 for ethene hydrogenation are −1.2, 0.85, and 1.0, respectively, for 0.08Rh-0.36Zn-DeAlBEA and −1.1, 0.90, and 1.0, respectively, for 0.08Rh-0.36Co-DeAlBEA. These values are similar to those reported for Rh/ReO_x-Al_2O_3[28] and $RhCo_3$/MCM-41.[9] The negative order in CO indicates that the adsorption of CO on Rh sites is stronger than the adsorption of C_2H_4 and H_2.[28,77−79] The reaction order in CO for ethene hydrogenation is also negative, consistent with the inference that hydrogenation also takes place on Rh centers.

DISCUSSION

Comparison of New Catalysts with Reported Supported Rhodium Hydroformylation Catalysts. Comparison the activity and selectivity of our catalysts with those of supported Rh-containing catalysts reported in previous studies (Table 3) is not straightforward because many of those were carried out at temperatures and reactant partial pressures different from ours. To compare our data with those reported

https://doi.org/10.1021/jacs.2c11075
J. Am. Chem. Soc. 2023, 145, 2911−2929

Table 3. Comparison of Ethylene Hydroformylation Activities of Various Supported Rh Catalysts

Catalyst	T/K	Reactant partial pressure/kPa			Propanal TOF/h^{-1}[a]	Propanal selectivity/%	Calculated propanal TOF_{RhZn}/h^{-1}[a,b]	Calculated propanal selectivity RhZn /%[c]	Calculated propanal TOF_{RhCo} /h^{-1}[a,d]	Calculated propanal selectivity RhCo/%[e]	Ref
		CO	C_2H_4	H_2							
Rh/2.9ReO_x-Al_2O_3	423	33.8	33.8	33.8	4	45	45	64	1281	59	28
Rh/$WO_{0.7}$-Al_2O_3	403	336	336	336	21	90	227	83	2652	67	39
Rh/MCM-41[f]	473	25	25	25	15.6/8.3	10.1	115	42	14760	48	34
$RhCo_3$/MCM-41[f]	473	25	25	25	62.4/62.4	32.6	30	43	2420	50	34
0.6Rh/SiO_2	453	252.2	252.2	252.5	954/342	38	667	65	40160	56	35
0.6Rh0.23Co/SiO_2	453	252.2	252.2	252.5	1283/578	46	667	65	40160	56	35
DPPTS-rhodium/SiO_2	393	336	336	336	55	N/A	166	86	1339	70	82
DPPPTS-RhAl1/SiO_2	393	336	336	336	134	N/A	166	86	1339	70	80
SILP-Cs-L/Rh10-IL30-Rh0.2	423	336	336	336	800	N/A	405	77	9450	63	81
0.08Rh-0.36Zn-DeAlBEA	403	33.8	33.8	11.3	12	79					This work
0.08Rh-0.36Co-DeAlBEA	403	33.8	33.8	11.3	153	69					This work

[a]All propanal TOFs are based on the total number of Rh atoms (i.e., the assumption that each Rh atom is accessible to reactants) with the exception of those for Rh/MCM-41, $RhCo_3$/MCM-41, 0.6Rh/SiO_2, and 0.6Rh0.23Co/SiO_2. The first value listed for those catalysts is based on the number of Rh sites accessible as determined by CO chemisorption and the assumption of a 1:1 CO:Rh stoichiometry, and the second value listed is based on the total number of Rh atoms. [b]Hydroformylation activity of 0.08Rh-0.36Zn-DeAlBEA calculated on the basis of the dependences of activity on reactant partial pressures and temperature presented in Table 2. [c]Hydroformylation selectivity of 0.08Rh-0.36Zn-DeAlBEA calculated on the basis of the dependences of activity on reactant partial pressures and temperature presented in Table 2. [d]Hydroformylation activity of 0.08Rh-0.36Co-DeAlBEA calculated on the basis of the dependences of activity on reactant partial pressures and temperature presented in Table 2. [e]Hydroformylation selectivity of 0.08Rh-0.36Co-DeAlBEA calculated on the basis of the dependences of activity on reactant partial pressures and temperature presented in Table 2. [f]Hydroformylation products are propanal together with propanol.

in the literature, we calculated the rates of reaction for our catalysts under the conditions used in each of the comparison investigations, using the rate parameters presented in Table 2. Further, various authors have used various bases for estimating the number of active sites in their catalysts. Most have scaled their estimated reaction rates of ethene consumption to the total number of Rh atoms in the catalyst (a good assumption when most of those atoms are exposed as mononuclear complexes or small clusters), and that is what we have done in evaluating our data. The exceptions are the data for Rh/MCM-41 and $RhCo_3$/MCM-41 (see refs 9 and 34) and Rh/SiO_2 and RhCo/SiO_2 (ref 35). The number of active Rh sites in each of those catalysts was estimated on the basis of CO chemisorption data, assuming a CO/Rh stoichiometry of unity. To place all entries in Table 3 on the same footing, we report the values of the propanal TOF based on the total number of Rh atoms.

As shown in Table 3, at identical reaction conditions 0.08Rh-0.36Co-DeAlBEA has a higher hydroformylation activity than any of the previously reported inorganically supported Rh catalysts, including those promoted with a metal oxide[9,21,28] or organic ligands.[80−82] The hydroformylation selectivity of our catalyst is also generally higher than those of the comparable catalysts. Table 3 also shows that the hydroformylation activity of 0.08Rh-0.36Zn-DeAlBEA (based on total Rh atoms) is higher than that of Rh/2.9ReO_x-Al_2O_3, Rh/$WO_{0.7}$-Al_2O_3, 0.6Rh0.23Co/SiO_2, DPPTS-Rh/SiO_2, and DPPPTS-$RhAl_1$/SiO_2, but is lower than that of $RhCo_3$/MCM-41 and SILP-Cs-L/Rh10-IL30-Rh0.2. It is also evident that under all the reaction conditions, the hydroformylation activity of 0.08Rh-0.36Zn-DeAlBEA is consistently lower than that of 0.08Rh-0.36Co-DeAlBEA by more than an order of magnitude, the exact value depending on the temperature and the partial pressures of the reactants.

As mentioned by Ro et al.,[39] at high reaction pressures, sintering of metal sites or changes in adsorbate coverage may occur, which will influence the reaction orders. The apparent activation energies may also change with temperature and pressure as a result of changes in the populations of adsorbed species. Therefore, for the most accurate comparisons, the pressure and temperature should not be markedly different from those selected for our determination of the reaction kinetics. Minimizing the differences minimizes the uncertainties involved in extracting the rate coefficients for ethene hydroformylation presented in Table 3.

Mechanism and Kinetics of Ethene Hydroformylation and Hydrogenation. The mechanism of alkene (e.g., ethene, propene) hydroformylation catalyzed by supported Rh has been investigated both experimentally and theoretically.[9,21,27,28,35,57,68,83,84] The reaction steps have typically been assumed to be analogous to those proposed for soluble Co complex catalysts by Heck and Breslow.[85] The first step in ethene hydroformylation involves ethene addition to a rhodium hydride, Rh−H, to form an ethyl ligand, followed

https://doi.org/10.1021/jacs.2c11075
J. Am. Chem. Soc. 2023, 145, 2911−2929

by insertion of CO to form an acyl (e.g., CH_3CH_2CO), and subsequent hydrogenation to form propanal. By contrast, alkene hydrogenation to the corresponding alkane occurs via hydrogenation of the alkyl intermediate.

The kinetics of ethene hydroformylation and hydrogenation on 0.08Rh-0.36Zn-DeAlBEA and 0.08Rh-0.36Co-DeAlBEA can be rationalized by the sequence of steps shown below, consistent with the proposal by Ro et al.[28] for ethene hydroformylation and hydrogenation on atomically dispersed supported Rh catalysts, Rh/Al_2O_3 and $Rh\text{-}ReO_x/Al_2O_3$.

$$H_2 + 2^* \leftrightarrow 2H \quad (1)$$

$$C_2H_4 + {}^* \leftrightarrow C_2H_4{}^* \quad (2)$$

$$C_2H_4{}^* + H{}^* \leftrightarrow C_2H_5{}^* + {}^* \quad (3)$$

$$C_2H_5{}^* + H{}^* \rightarrow C_2H_6{}^* + {}^* \quad (4)$$

$$C_2H_6{}^* \leftrightarrow C_2H_6 + {}^* \quad (5)$$

$$CO + {}^* \leftrightarrow CO{}^* \quad (6)$$

$$C_2H_5{}^* + CO{}^* \leftrightarrow C_3H_5O{}^* + {}^* \quad (7)$$

$$C_3H_5O{}^* + H{}^* \leftrightarrow C_3H_6O{}^* + {}^* \quad (8)$$

$$C_3H_6O{}^* \leftrightarrow C_3H_6O + {}^* \quad (9)$$

Steps 1−5 describe ethane formation, and steps 1−3 and 6−9 propanal formation. Earlier work suggests that the rate-determining step in alkene hydroformylation depends on the composition of the alkene,[9] the reaction conditions,[84] and the catalyst.[27,86] CO insertion to form an acyl,[28,35,38,58] hydrogenation of the acyl,[68,83,84] and coordination of CO[27] have all been proposed as possible rate-determining steps. Moreover, it has recently been suggested[9] that both CO insertion and acyl hydrogenation can be kinetically relevant. By contrast, for ethane formation, the rate-determining step is generally identified as the hydrogenation of the alkyl ligand.[9,85,84]

The H/D KIE value characterizing ethene hydroformylation on 0.08Rh-0.36Co-DeAlBEA is 1.7, whereas that for 0.08Rh-0.36Zn-DeAlBEA is only 1.2. The comparison suggests that hydrogenation of acyl species, Step 8, contributes more to the formation of propanal on 0.08Rh-0.36Co-DeAlBEA than on 0.08Rh-0.36Zn-DeAlBEA. This inference is supported by the higher reaction order in H_2 for the former vs the latter catalyst (Table 2). It is also notable that for both catalysts ethyl migration and addition to the Rh−CO moiety are also kinetically important in propanal formation, as suggested by the IR spectra (Figure 6A and B). Therefore, for both catalysts, we suggest that formation of acyl species and their subsequent reduction are kinetically significant in propanal formation. However, the data are not sufficient for a quantitative assessment of the relative importance of Steps 7 and 8 to the overall reaction kinetics.

It is notable that the reaction orders in H_2, CO, and C_2H_4 for ethane formation on 0.08Rh-0.36Zn-DeAlBEA and 0.08Rh-0.36Co-DeAlBEA are more nearly comparable to each other than the reaction orders for propanal formation (Table 2). This finding suggests that the rate-limiting step is likely to be Step 4 for both catalysts.

Equations 10 and 11 are rate expressions for propanal formation assuming that either Step 7 or Step 8 is rate limiting, respectively, and eq 12 is the rate expression for ethane formation. All of these expressions are derived in Section S1 of the Supporting Information.

$$r_{propanal} = \frac{k_{C3H5O}k_{C2H5}K_{C2H4}\sqrt{K_{H2}}K_{CO}[C_2H_4][CO]\sqrt{[H_2]}}{(K_{CO}[CO] + K_{C2H5}K_{C2H4}\sqrt{K_{H2}}[C_2H_4]\sqrt{[H_2]} + k_{C3H5O}k_{C2H5}K_{C2H4}\sqrt{K_{H2}}K_{CO}[C_2H_4]\sqrt{[H_2]}[CO])^2} \quad (10)$$

$$r_{propanal} = \frac{k_{C3H6O}k_{C3H5O}k_{C2H5}K_{C2H4}K_{H2}K_{CO}[C_2H_4][H_2][CO]}{(K_{CO}[CO] + K_{C2H5}K_{C2H4}\sqrt{K_{H2}}[C_2H_4]\sqrt{[H_2]} + k_{C3H5O}k_{C2H5}K_{C2H4}\sqrt{K_{H2}}K_{CO}[C_2H_4]\sqrt{[H_2]}[CO])^2} \quad (11)$$

$$r_{ethane} = \frac{k_{C2H6}k_{C2H5}K_{C2H4}K_{H2}[C_2H_4][H_2]}{(K_{CO}[CO] + K_{C2H5}K_{C2H4}\sqrt{K_{H2}}[C_2H_4]\sqrt{[H_2]} + k_{C3H5O}k_{C2H5}K_{C2H4}\sqrt{K_{H2}}K_{CO}[C_2H_4]\sqrt{[H_2]}[CO])^2} \quad (12)$$

Equations 10−12 are based on the Langmuirian assumption of uniform catalytic sites. In these equations, k_i represents the forward rate coefficients of the respective elementary reactions 1−9, K_i is the equilibrium constant for reaction i, and [X] is the gas-phase concentration of species X. Equations 10 and 11 show that the only difference is that dependence of rate on the partial pressure of H_2 is half-order if Step 7 is rate-limiting and first-order if Step 8 is rate-limiting. The experimentally observed dependence of rate on H_2 partial pressure for 0.08Rh-0.36Zn-DeAlBEA is 0.67, whereas it is 0.75 for 0.08Rh-0.36Co-DeAlBEA. Because both orders are greater than 0.5 but less than 1.0, the results suggest that Step 8 is kinetically important for reaction on each catalyst. This inference is also consistent with the observed H/D KIE values.

Of further significance is that the negative reaction order in CO for each catalyst is substantially greater in magnitude than unity, whereas a value of −1 would be expected if the most abundant surface species were adsorbed CO. The values are −0.56 for 0.08Rh-0.36Zn-DeAlBEA and −0.81 for 0.08Rh-0.36Co-DeAlBEA. This comparison implies that the coverages of Rh sites by ethyl and acyl groups are significant, an inference supported by the IR spectra shown in Figure 6A and B. The data further imply that CO is somewhat more strongly bound on the latter catalyst, but the weaker inhibition of propanal formation by CO on 0.08Rh-0.36Zn-DeAlBEA may also arise from the greater importance of acyl species relative to adsorbed CO on this catalyst. Two observations support this latter suggestion, the first being the greater intensity of the IR band at 1617 cm^{-1} (attributed to propionyl species observed in Figure 6B) relative to that observed for 0.08Rh-0.36Zn-DeAlBEA (Figure 6A). The second observation is the stronger growth in the intensity of the IR band observed at 1617 cm^{-1} when the partial pressure of H_2 was increased from 3.4 to 45 kPa, which is what would be expected by inspection of the third term in the denominator of eq 10 or 11.

Equation 12 suggests that the dependence of the rate of ethane formation on the partial pressures of H_2 and C_2H_4 should be identical to those appearing in eq 11, because the denominators of eqs 11 and 12 are identical. But the information presented in Table 1 shows that the rate dependences on the partial pressures of H_2 and C_2H_4 are nearly the same for the two catalysts (∼1.0 and ∼0.9), and the dependence on CO partial pressure is −1.0 for each. It is notable that these are just what would be expected if ethene

https://doi.org/10.1021/jacs.2c11075
J. Am. Chem. Soc. 2023, 145, 2911−2929

hydrogenation were occurring on Rh sites for which CO is the most abundant adsorbed species. The fact that both partial pressure dependences are the same for the two catalysts and substantially different from those for propanal formation on each catalyst suggests that ethene hydrogenation occurs on Rh sites that do not interact, or interact minimally, with either Zn or Co atoms, such as would be expected for Rh nanoparticles.

Effect of M-DeAlBEA Support on Ethene Hydroformylation. The observed differences in the promoting effects of Zn and Co on the ethene hydroformylation activity of Rh are attributed in part to the effectiveness of ≡SiOCoOH and ≡SiOZnOH groups in favoring the dispersion of the Rh. IR spectra of adsorbed CO and Rh EXAFS data indicate that Rh atoms are more highly dispersed on 0.36Co-DeAlBEA than on 0.36Zn-DeAlBEA. Because the fraction of Rh atoms accessible for reaction increases with Rh dispersion, one expects the rate of hydroformylation to increase accordingly. However, Rh dispersion alone cannot account for the different influences of Co and Zn, because 0.08Rh-0.36Zn-DeAlBEA and 0.08Rh-0.36Co-DeAlBEA exhibit differences in the H/D KIE and the rate parameters, particularly the apparent activation energy. Therefore, one also needs to consider effects of Zn and Co on the electronic properties of Rh. Investigations of intermetallic Pt_1M_1 alloys indicate that electron donation from Zn to Pt is greater than that from Co.[87] Similar effects are therefore expected for Rh. We propose that changes in the electronic properties of the Rh centers influence its hydroformylation activity by altering the nature of the rate-limiting step. Consistent with this hypothesis, it is has been observed that increasing the electron-withdrawing tendency of the ligands in a molecular Rh complex increases its hydroformylation activity[86,88−96] and that the rate-determining step for such complexes is hydrogenolysis of the acyl group.[97−99] By contrast, for electron-rich Rh centers, the rate of hydroformylation is controlled by the rate of acyl group formation via alkyl migration to CO. Therefore, the lower hydroformylation activity of 0.08Rh-0.36Zn-DeAlBEA compared with 0.08Rh-0.36Co-DeAlBEA can be attributed, at least in part, to the higher electron density on Rh on the former catalyst, for which the Rh−CO interaction is too strong, hence inhibiting ethyl group migration to CO to form acyl groups. The electron density on Rh in 0.08Rh-0.36Co-DeAlBEA is expected to be lower, and consequently the generation of acyl groups is expected to be more facile, which would enhance its hydroformylation activity. Although the CO-IR experiments did not provide clear evidence of a change that would imply different electronic properties of Rh due to Zn−Rh and Co−Rh contacts in the nested Zn−Rh and Co−Rh clusters within the zeolite, this interpretation of the effects of Zn and Co is consistent with the proposed mechanism and our interpretation of the H/D KIE, which suggests that acyl formation is the more important step kinetically limiting hydroformylation on 0.08Rh-0.36Zn-DeAlBEA and that hydrogenation of acyl is the more important step kinetically limiting hydroformylation on 0.08Rh-0.36Co-DeAlBEA. Another possible reason for the higher hydroformylation activity of 0.08Rh-0.36Co-DeAlBEA than of 0.08Rh-0.36Zn-DeAlBEA is that Co may directly participate in the ethene hydroformylation process. However, on the basis of reported work on ethene hydroformylation catalyzed by $RhCo_3$/MCM-41 and $RhCo/SiO_2$,[34,35] we suggest that the majority of Co species that interact strongly with the siliceous supports adsorbed CO only weakly and were not active for this process, consistent with our experimental results showing that both Zn-DeAlBEA and Co-DeAlBEA lack activity for ethene hydroformylation under our conditions. Moreover, literature reports[34,35] include data suggesting that when Rh−Co species are generated, they are characterized by weaker Rh−CO bonds than Rh species and favor CO migration and insertion into adsorbed ethyl species, a key step in ethene hydroformylation and consistent with our interpretation.

CONCLUSIONS

The results presented here show that Rh can be highly dispersed on dealuminated zeolite BEA (DeAlBEA) containing clusters (4−6 units) of either ≡SiOZn−OH or ≡SiOCo−OH groups. EXAFS and IR spectra of adsorbed CO show that Rh is present as a combination of atomically dispersed species and nanoclusters and that the proportion of the former increases significantly with increasing M/Rh ratio (M = Zn or Co). Rh-Zn-DeAlBEA and Rh-Co-DeAlBEA are highly active and selective for ethene hydroformylation; the TOF for propanal formation increases with increasing M/Rh ratio, roughly correlated with the fraction of Rh that is atomically dispersed. For a fixed set of reaction conditions, the TOF for ethene hydroformylation on Rh-Co-DeAlBEA is roughly 15-fold higher than that for Rh-Zn-DeAlBEA, whereas the selectivity to propanal is only slightly greater for Rh-Zn-DeAlBEA. Under identical reaction conditions, the ethene hydroformylation activity of Rh-Co-DeAlBEA exceeds that of all previously reported Rh-containing catalysts involving inorganic supports. The higher activity of the Co- than of the Zn-containing catalyst is attributed to the somewhat higher atomic dispersion of Rh in Rh-Co-DeAlBEA and to the less polarizing effect of Rh−Co vs Rh−Zn bonds. Notably, EXAFS data characterizing Rh-Co-DeAlBEA under reaction conditions show that the dispersion of Rh increases relative to that observed following H_2 reduction, as a consequence of the oxidative fragmentation of Rh clusters by CO. Reaction orders for ethene hydroformylation to propanal and hydrogenation to ethane are positive in ethene and in H_2 but negative in CO. These reaction orders suggest that hydroformylation occurs mainly on slightly positively charged, atomically dispersed Rh, the properties of which are affected by Rh−M (M = Zn or Co) contacts, and that, by contrast, hydrogenation occurs mainly on zerovalent Rh nanoclusters. These inferences are supported by the observed trends in propanal selectivity with M/Rh ratio. *In situ* IR spectra suggest that propanal is produced via formation and subsequent hydrogenation of propionyl groups and that the formation of these species may be preceded by formation of an agnostic, cyclic acyl intermediate. The observed H/D KIE effect and reaction kinetics suggest that the formation of propanal is rate-limited by a combination of acyl formation and reductions, the first of these processes being more important for Rh-Zn-DeAlBEA, and the second for Rh-Co-DeAlBEA. The insights gained from this investigation indicate that atomic dispersion of Rh stabilized by multiple interactions with Co cations results in exceptionally active catalysts for ethene hydroformylation.

EXPERIMENTAL METHODS

Catalyst Preparation. Zn-DeAlBEA, Co-DeAlBEA, and Rh-DeAlBEA were prepared via two-step processes consisting of dealumination of zeolite H-Beta and subsequent introduction of zinc, cobalt, or rhodium species by aqueous impregnation with $Zn(NO_3)_2{\cdot}6H_2O$ (Alfa Aesar, 99% metal basis), $Co(NO_3)_2{\cdot}6H_2O$, or $Rh(NO_3)_3{\cdot}xH_2O$ (Sigma-Aldrich), respectively. In a typical synthesis,

https://doi.org/10.1021/jacs.2c11075
J. Am. Chem. Soc. 2023, 145, 2911−2929

zeolite H-Beta (provided by BASF) with a Si/Al ratio of 13 (atomic, determined by ICP analysis) was suspended in aqueous 13 M nitric acid at 373 K and stirred for 20 h to make DeAlBEA. The resulting powder was filtered, washed with MQ deionized water until a pH of 6−7 was reached, and then dried at 373 K under vacuum overnight. Essentially complete removal of Al by this procedure was confirmed by ^{27}Al NMR spectroscopy of the solid.[46,49] DeAlBEA was then impregnated with an aqueous metal nitrate solution. Specifically, the molar concentrations of Zn^{2+}, Co^{2+}, and Rh^{3+} solutions were 0.044, 0.087, and 0.13 mol/L to achieve metal (M)/Al ratios (mol of metal introduced per mol of Al in zeolite H-Beta prior to dealumination) of 0.12, 0.24, and 0.36, respectively. Generally, 1.4 mL of solution was needed for 0.5 g of DeAlBEA. The resulting slurry was dried at room temperature and then further dried at 353 K under vacuum for 2 h. The powder was ground for 20 min, and then the Zn- or Co-containing zeolite was calcined in nitrogen at 823 K for 6 h, and the only Rh-containing catalyst was calcined at 673 K for 2 h. The final product is designated as M-DeAlBEA, where x indicates the M/Al ratio (e.g., 0.36Zn-DeAlBEA means the Zn/Al ratio is 0.36). Essentially all of the aluminum in zeolite H-BEA was removed by dealumination to produce silanol nests, each containing approximately four ≡Si−OH groups.[46] Therefore, M/Al represents the average number of metal atoms per silanol nest (i.e., four ≡Si−OH groups).

Rh-Zn-DeAlBEA and Rh-Co-DeAlBEA were prepared by using Zn-DeAlBEA and Co-DeAlBEA as supports, respectively. Rhodium was introduced via aqueous impregnation of each support using $Rh(NO_3)_3{\cdot}xH_2O$ (Sigma-Aldrich). The molar concentrations of Rh^{3+} solutions were 0.00073, 0.00146, and 0.0292, chosen to achieve Rh/Al ratios (mol of Rh introduced per mol of Al in zeolite H-Beta prior to dealumination) of 0.02, 0.04, and 0.08, respectively. Generally, 1.4 mL of solution was needed for 0.5 g of Zn/Co-DeAlBEA. The resulting slurry was dried at room temperature and then further dried at 353 K for 2 h. The powder mixture was ground for 20 min, and then the catalyst was calcined in nitrogen at 673 K for 2 h. The final products are designated as xRh-yZn-DeAlBEA and xRh-yCo-DeAlBEA, where x and y stand for the M/Al ratios and where Al refers to the original amount of Al in BEA prior to dealumination.

Catalyst Characterization. Fourier transform IR (FTIR) spectra were acquired using a Thermo Scientific Nicolet 6700 spectrometer equipped with a liquid-nitrogen-cooled MCT detector. All samples for IR experiments (~30 mg) were pressed into thin wafers and transferred into a stainless-steel sample holder, which was then placed into a Harrick high-temperature cell equipped with CaF_2 windows.[100] To obtain spectra in the hydroxyl stretching region, a spectrum of the empty cell was used as the background, whereas for spectra of adsorbed pyridine, the spectrum of the sample pellet taken prior to pyridine adsorption was used as the background. To determine spectra of the catalysts, the material was pressed into a thin 20-mm-diameter self-supporting wafer (compressed at 25,000 psi) and then transferred into the transmission cell. For IR spectroscopy of adsorbed pyridine and 2,6-di-*tert*-butylpyridine, a wafer of the catalyst was pretreated in flowing He at 773 K for 1 h and then cooled to 393 K prior to acquisition of spectra; 2 μL of pyridine or 2,6-di-*tert*-butylpyridine was injected for each experiment, and then the sample cell was purged with He for 20 or 60 min to remove physisorbed species. To characterize the dispersion of Rh, IR spectra were recorded after adsorption of CO (3 kPa) at atmospheric pressure. Each catalyst was first reduced for 1 h at 473 K in a stream of 30 mL(NTP)/min of 10% H_2 balanced with He at atmospheric pressure. A baseline spectrum was taken before CO was introduced at 303 K. Then 3% CO/97% He with a total flow rate of 100 mL(NTP)/min was introduced to the catalyst, and the flow rate was maintained until a maximum spectral intensity was achieved (~20 min). Thereafter, the cell was purged with 100 mL(NTP)/min of He for 20 min. Each spectrum was obtained by averaging 64 sequentially collected scans at a resolution of 4 cm^{-1}. In *in situ* IR experiments, each catalyst was reduced in a stream of 30 mL(NTP)/min 10% H_2 balanced with He at atmospheric pressure and 473 K for 1 h and then cooled to 403 K to collect a baseline spectrum.

Powder X-ray diffraction (PXRD) patterns of catalysts were acquired with a Bruker D8 GADDS diffractometer equipped with a Cu Kα source (40 kV, 40 mA). BET surface areas were calculated from nitrogen adsorption isotherms obtained using a Micromeritics Gemini VII 2390 surface area analyzer. The Rh, Zn, and Co loadings were determined by inductively coupled plasma analysis; the elemental analyses were performed by Galbraith Laboratories, Inc.

Rh K-edge and Co K-edge XA spectra of the samples were recorded at beamline 4-1 of the Stanford Synchrotron Radiation Lightsource (SSRL). For Rh K-edge measurements, XANES and EXAFS spectra were collected in fluorescence detection mode with a PIPS detector to characterize samples in flowing gases. Energy calibration was done with a Rh reference foil mounted down-beam of the sample that was simultaneously scanned with the sample. Approximately 40 mg of each solid sample, 0.08Rh-0.36Zn-DeAlBEA and 0.08Rh-0.36Co-DeAlBEA, was packed in a 3 mm inside-diameter quartz capillary cell/flow reactor. EXAFS data characterizing the as-synthesized samples were collected at 298 K in flowing He. Continuous near-edge spectra were collected during subsequent treatment of each catalyst in flowing 10% H_2 in He as the temperature was ramped from 298 K to 473 K at a rate of 10 K/min. This measurement was followed by a dwell of 1 h at 473 K with the sample in 10% H_2 in He. The catalyst was then cooled to 298 K before characterization of the treated sample by EXAFS spectroscopy, with multiple scans recorded. In another experiment, the 0.08Rh-0.36Co-DeAlBEA was treated at 473 K in 10% H_2 in He for 1 h (with a temperature ramp from room temperature at 10 K/min) followed by cooling to 388 K and introduction of a stream of reactants to undergo ethyne hydroformylation ($H_2/CO/C_2H_4$/He = 2.2/6.6/2.2/9). After a dwell at 388 K for 1 h, the sample was cooled to 298 K with the same gas flowing, followed by switching the gas to He. Rh K-edge EXAFS spectra were collected at each of the above conditions. For Co K-edge XAS measurements, approximately 4 mg of 0.08Rh-0.36Co-DeAlBEA was packed in a 1 mm inside-diameter quartz capillary cell/flow reactor. XANES data were collected in transmission detection mode for samples in flowing gases. XANES data characterizing the as-synthesized sample in flowing He were collected at 298 K. This procedure was followed by treatment of the catalyst in 10% H_2 in He for 1 h at 473 K.

Athena and Artemis software, parts of the Demeter package,[101] were used for analysis of the EXAFS data. Preprocessing of data including alignment, edge calibration, normalization, and background subtraction was done with Athena. The energy at the Rh K-edge and at the Co K-edge were determined by the first inflection point of the absorption edge data characterizing the reference Rh foil (calibrated to the reported energy, 23,220.0 eV) and Co foil (calibrated to the reported energy, 7709.0 eV), respectively. Standard procedures were used in the analysis of the XANES data.[101] Fitting of EXAFS data was carried out in Artemis considering k^1-, k^2-, and k^3-weightings (k is the wave vector). The fitting ranges in both k space and R space (R is distance) in analysis of data characterizing each as-synthesized, pretreated, and postcatalytic reaction sample were determined by the data quality, according to conventional methods.

Measurement of Catalytic Activity and Selectivity. Catalytic activity and selectivity data were acquired with samples in a quartz packed-bed, once-through downflow reactor (10 mm inside diameter) operated at atmospheric pressure. Quartz wool was placed below the catalyst bed to hold it in place. The reactor temperature was maintained using a tube furnace equipped with a Watlow temperature controller and a K-type thermocouple sensor. Prior to reaction, the catalyst was heated at a rate of 10 K min^{-1} to 473 K in flowing 10% H_2 balanced with helium at a flow rate of 20 mL(NTP) min^{-1} and held for 60 min before the temperature was adjusted to the reaction temperature.

■ ASSOCIATED CONTENT

Supporting Information

The Supporting Information is available free of charge at https://pubs.acs.org/doi/10.1021/jacs.2c11075.

https://doi.org/10.1021/jacs.2c11075
J. Am. Chem. Soc. 2023, 145, 2911−2929

Derivation of rate expression for ethene hydroformylation and supplementary data (XRD, BET, ICP, FTIR, and XAS) (Figures S1−S14, Tables S1−S5) (PDF)

AUTHOR INFORMATION

Corresponding Author

Alexis T. Bell − *Lawrence Berkeley National Laboratory, Berkeley, California 94720, United States; Department of Chemical and Biomolecular Engineering, University of California, Berkeley, California 94720, United States;* orcid.org/0000-0002-5738-4645; Email: alexbell@berkeley.edu

Authors

Liang Qi − *Lawrence Berkeley National Laboratory, Berkeley, California 94720, United States; Department of Chemical and Biomolecular Engineering, University of California, Berkeley, California 94720, United States; National Engineering Laboratory for Methanol to Olefins, Dalian National Laboratory for Clean Energy, Dalian Institute of Chemical Physics, Chinese Academy of Sciences, Dalian 116023, China*

Sonali Das − *Department of Chemical Engineering, University of California, Davis, California 95616, United States*

Yanfei Zhang − *Lawrence Berkeley National Laboratory, Berkeley, California 94720, United States; Department of Chemical and Biomolecular Engineering, University of California, Berkeley, California 94720, United States; College of Environmental Science and Engineering, Dalian Maritime University, Dalian 116026, China*

Danna Nozik − *Lawrence Berkeley National Laboratory, Berkeley, California 94720, United States; Department of Chemical and Biomolecular Engineering, University of California, Berkeley, California 94720, United States*

Bruce C. Gates − *Department of Chemical Engineering, University of California, Davis, California 95616, United States;* orcid.org/0000-0003-0274-4882

Complete contact information is available at: https://pubs.acs.org/10.1021/jacs.2c11075

Author Contributions

L.Q., S.D., and Y.Z. contributed equally to this work. L.Q., S.D., and Y.Z. performed catalyst preparation, measurements of reaction kinetics, acquisition of X-ray absorption data, and data interpretation. B.C.G. assisted in the interpretation of the X-ray absorption data. A.T.B. supervised the project. All authors discussed the results and participated in the preparation of the manuscript.

Notes

The authors declare no competing financial interest.

ACKNOWLEDGMENTS

A.T.B., L.Q., and Y.Z. acknowledge support for this work by the Office of Science, Office of Basic Energy Sciences, of the U.S. Department of Energy (DOE) under Contract No. DE-AC02-05CH11231. B.C.G. and S.D. acknowledge support for their contributions to this work by DOE, BES, under Contract DE-SC0012702 (an Energy Frontier Research Center supporting the Inorganometallic Catalyst Design Center). All authors acknowledge use of the Stanford Synchrotron Radiation Light Source (SSRL), SLAC National Accelerator Laboratory, which is supported by the DOE, BES, under Contract No. DE-AC02-76SF00515. Additional support by the Consortium for Operando and Advanced Catalyst Characterization via Electronic Spectroscopy and Structure (CoACCESS) at SLAC is acknowledged. CoACCESS is supported by DOE, BES, Chemical Sciences, Geosciences and Biosciences, under Contract DE-AC02-76SF00515. L.Q. also acknowledges support from the Dalian Institute of Chemical Physics, Chinese Academy of Sciences, People's Republic of China.

REFERENCES

(1) Hanf, S.; Rupflin, L. A.; Glaser, R.; Schunk, S. A. Current State of the Art of the Solid Rh-Based Catalyzed Hydroformylation of Short-Chain Olefins. *Catalysts* **2020**, *10* (5), 510−546.

(2) Li, C.; Wang, W.; Yan, L.; Ding, Y. A mini review on strategies for heterogenization of rhodium-based hydroformylation catalysts. *Front. Chem. Sci. Eng.* **2018**, *12* (1), 113−123.

(3) Franke, R.; Selent, D.; Börner, A. Applied hydroformylation. *Chem. Rev.* **2012**, *112* (11), 5675−5732.

(4) Liu, B. Y.; Huang, N.; Wang, Y.; Lan, X. C.; Wang, T. F. Promotion of Inorganic Phosphorus on Rh Catalysts in Styrene Hydroformylation: Geometric and Electronic Effects. *ACS Catal.* **2021**, *11* (3), 1787−1796.

(5) Navidi, N.; Thybaut, J. W.; Marin, G. B. Experimental investigation of ethylene hydroformylation to propanal on Rh and Co based catalysts. *Appl. Catal. A-Gen.* **2014**, *469*, 357−366.

(6) Jiao, Y.; Torne, M. S.; Gracia, J.; Niemantsverdriet, J. H.; van Leeuwen, P. W. Ligand effects in rhodium-catalyzed hydroformylation with bisphosphines: steric or electronic? *Catal. Sci. Technol.* **2017**, *7* (6), 1404−1414.

(7) Clark, T. P.; Landis, C. R.; Freed, S. L.; Klosin, J.; Abboud, K. A. Highly active, regioselective, and enantioselective hydroformylation with Rh catalysts ligated by bis-3, 4-diazaphospholanes. *J. Am. Chem. Soc.* **2005**, *127* (14), 5040−5042.

(8) Delolo, F. G.; dos Santos, E. N.; Gusevskaya, E. V. Anisole: a further step to sustainable hydroformylation. *Green Chem.* **2019**, *21* (5), 1091−1098.

(9) Mao, Z.; Xie, Z.; Chen, J. G. Comparison of Heterogeneous Hydroformylation of Ethylene and Propylene over $RhCo_3$/MCM-41 Catalysts. *ACS Catal* **2021**, *11*, 14575−14585.

(10) Amsler, J.; Sarma, B. B.; Agostini, G.; Prieto, G.; Plessow, P. N.; Studt, F. Prospects of Heterogeneous Hydroformylation with Supported Single Atom Catalysts. *J. Am. Chem. Soc.* **2020**, *142* (11), 5087−5096.

(11) Cole-Hamilton, D. J. Homogeneous catalysis–new approaches to catalyst separation, recovery, and recycling. *Science* **2003**, *299* (5613), 1702−1706.

(12) Ichikawa, M. Catalytic hydroformylation of olefins over the rhodium, bimetallic RhCo, and cobalt carbonyl clusters supported with some metal oxides. *J. Catal.* **1979**, *59* (1), 67−78.

(13) Kim, T.; Celik, F. E.; Hanna, D. G.; Shylesh, S.; Werner, S.; Bell, A. T. Gas-Phase Hydroformylation of Propene over Silica-Supported PPh_3-Modified Rhodium Catalysts. *Top Catal.* **2011**, *54* (5), 299−307.

(14) Sun, Q.; Dai, Z.; Liu, X.; Sheng, N.; Deng, F.; Meng, X.; Xiao, F.-S. Highly efficient heterogeneous hydroformylation over Rh-metalated porous organic polymers: synergistic effect of high ligand concentration and flexible framework. *J. Am. Chem. Soc.* **2015**, *137* (15), 5204−5209.

(15) Li, C.; Xiong, K.; Yan, L.; Jiang, M.; Song, X.; Wang, T.; Chen, X.; Zhan, Z.; Ding, Y. Designing highly efficient Rh/CPOL-bp&PPh_3 heterogenous catalysts for hydroformylation of internal and terminal olefins. *Catal. Sci. Technol.* **2016**, *6* (7), 2143−2149.

(16) Li, C.; Yan, L.; Lu, L.; Xiong, K.; Wang, W.; Jiang, M.; Liu, J.; Song, X.; Zhan, Z.; Jiang, Z. Single atom dispersed Rh-Biphephos&PPh_3@porous organic copolymers: highly efficient catalysts for continuous fixed-bed hydroformylation of propene. *Green Chem.* **2016**, *18* (10), 2995−3005.

(17) Li, C.; Sun, K.; Wang, W.; Yan, L.; Sun, X.; Wang, Y.; Xiong, K.; Zhan, Z.; Jiang, Z.; Ding, Y. Xantphos doped Rh/POPs-PPh_3 catalyst for highly selective long-chain olefins hydroformylation: chemical and DFT insights into Rh location and the roles of Xantphos and PPh_3. *J. Catal.* **2017**, *353*, 123−132.
(18) Wang, Y.; Yan, L.; Li, C.; Jiang, M.; Zhao, Z.; Hou, G.; Ding, Y. Heterogeneous Rh/CPOL-BP&$P(OPh)_3$ catalysts for hydroformylation of 1-butene: The formation and evolution of the active species. *J. Catal.* **2018**, *368*, 197−206.
(19) Jia, X.; Liang, Z.; Chen, J.; Lv, J.; Zhang, K.; Gao, M.; Zong, L.; Xie, C. Porous organic polymer supported rhodium as a reusable heterogeneous catalyst for hydroformylation of olefins. *Org. Lett.* **2019**, *21* (7), 2147−2150.
(20) Liu, B.; Wang, Y.; Huang, N.; Lan, X.; Wang, T. Activity Promotion of $Rh_{8-x}Co_xP_4$ Bimetallic Phosphides in Styrene Hydroformylation: Dual Influence of Adsorption and Surface Reaction. *ACS Catal.* **2021**, *11* (15), 9850−9859.
(21) Liu, B.; Huang, N.; Wang, Y.; Lan, X.; Wang, T. Insights into the Activity Screening and Hydroformylation Kinetics of Rh-Based Bimetallic Phosphides. *ACS Catal.* **2021**, *11*, 15235−15243.
(22) Rupflin, L. A.; Mormul, J.; Lejkowski, M.; Titlbach, S.; Papp, R.; Glaser, R.; Dimitrakopoulou, M.; Huang, X.; Trunschke, A.; Willinger, M. G.; Schlogl, R.; Rosowski, F.; Schunk, S. A. Platinum Group Metal Phosphides as Heterogeneous Catalysts for the Gas-Phase Hydroformylation of Small Olefins. *ACS Catal.* **2017**, *7* (5), 3584−3590.
(23) Marinkovic, J. M.; Riisager, A.; Franke, R.; Wasserscheid, P.; Haumann, M. Fifteen years of supported ionic liquid phase-catalyzed hydroformylation: material and process developments. *Ind. Eng. Chem. Res.* **2019**, *58* (7), 2409−2420.
(24) Weiß, A.; Giese, M.; Lijewski, M.; Franke, R.; Wasserscheid, P.; Haumann, M. Modification of nitrogen doped carbon for SILP catalyzed hydroformylation of ethylene. *Catal. Sci. Technol.* **2017**, *7* (23), 5562−5571.
(25) Gadge, S. T.; Bhanage, B. M. Recent developments in palladium catalysed carbonylation reactions. *RSC Adv.* **2014**, *4* (20), 10367−10389.
(26) Coufourier, S.; Gaillard, S.; Clet, G.; Serre, C.; Daturi, M.; Renaud, J.-L. A MOF-assisted phosphine free bifunctional iron complex for the hydrogenation of carbon dioxide, sodium bicarbonate and carbonate to formate. *Chem. Commun.* **2019**, *55* (34), 4977−4980.
(27) Lee, S.; Patra, A.; Christopher, P.; Vlachos, D. G.; Caratzoulas, S. Theoretical Study of Ethylene Hydroformylation on Atomically Dispersed Rh/Al_2O_3 Catalysts: Reaction Mechanism and Influence of the ReO_x Promoter. *ACS Catal.* **2021**, *11* (15), 9506−9518.
(28) Ro, I.; Xu, M. J.; Graham, G. W.; Pan, X. Q.; Christopher, P. Synthesis of Heteroatom Rh-ReO_x Atomically Dispersed Species on Al_2O_3 and Their Tunable Catalytic Reactivity in Ethylene Hydroformylation. *ACS Catal.* **2019**, *9* (12), 10899−10912.
(29) Wang, L. B.; Zhang, W. B.; Wang, S. P.; Gao, Z. H.; Luo, Z. H.; Wang, X.; Zeng, R.; Li, A. W.; Li, H. L.; Wang, M. L.; Zheng, X. S.; Zhu, J. F.; Zhang, W. H.; Ma, C.; Si, R.; Zeng, J. Atomic-level insights in optimizing reaction paths for hydroformylation reaction over Rh/CoO single-atom catalyst. *Nat. Commun.* **2016**, *7*, 14036−14044.
(30) Lang, R.; Li, T. B.; Matsumura, D.; Miao, S.; Ren, Y. J.; Cui, Y. T.; Tan, Y.; Qiao, B. T.; Li, L.; Wang, A. Q.; Wang, X. D.; Zhang, T. Hydroformylation of Olefins by a Rhodium Single-Atom Catalyst with Activity Comparable to $RhCl(PPh_3)(_3)$. *Angew. Chem., Int. Ed.* **2016**, *55* (52), 16054−16058.
(31) Ichikawa, M.; Rao, L.-F.; Kimura, T.; Fukuoka, A. Heterogenized bimetallic clusters: Their structures and bifunctional catalysis. *J. Mol. Catal.* **1990**, *62* (1), 15−35.
(32) Fukuoka, A.; Rao, L.-F.; Kosugi, N.; Kuroda, H.; Ichikawa, M. Selective hydroformylation of ethene and propene catalysed on nay zeolite-entrapped Rh_6 and bimetallic RhFe clusters and their structural characterization by extended x-ray absorption fine structure and Fourier transform infrared spectroscopy. *Appl. Catal.* **1989**, *50* (1), 295−301.
(33) Trunschke, A.; Böttcher, H.-C.; Fukuoka, A.; Ichikawa, M.; Miessner, H. Olefin hydroformylation and selective hydrogenation of acetaldehyde on Mo-promoted Rh/SiO_2 catalysts derived from metal salt and heteronuclear cluster precursors. *Catal. Lett.* **1991**, *8* (2), 221−228.
(34) Xie, Z.; Xu, Y.; Xie, M.; Chen, X.; Lee, J. H.; Stavitski, E.; Kattel, S.; Chen, J. G. Reactions of CO_2 and ethane enable CO bond insertion for production of C_3 oxygenates. *Nat. Commun.* **2020**, *11* (1), 1−8.
(35) Huang, N.; Liu, B. Y.; Lan, X. C.; Wang, T. F. Insights into the Bimetallic Effects of a RhCo Catalyst for Ethene Hydroformylation: Experimental and DFT Investigations. *Ind. Eng. Chem. Res.* **2020**, *59* (42), 18771−18780.
(36) Huang, L. Formation of bimetallic $RhCo_3$ clusters from monometallic carbonyl clusters on SiO_2 as probed by hydroformylation. *J. Mol. Catal. A: Chem.* **1997**, *125* (1), 47−52.
(37) Chen, M.; Gupta, G.; Ordonez, C. W.; Lamkins, A. R.; Ward, C. J.; Abolafia, C. A.; Zhang, B.; Roling, L. T.; Huang, W. Intermetallic Nanocatalyst for Highly Active Heterogeneous Hydroformylation. *J. Am. Chem. Soc.* **2021**, *143* (49), 20907−20915.
(38) Ichikawa, M.; Lang, A.; Shriver, D.; Sachtler, W. Selective hydroformylation of ethylene on rhodium-zinc-silica. An apparent example of site isolation of rhodium and Lewis acid-promoted carbonyl insertion. *J. Am. Chem. Soc.* **1985**, *107* (24), 7216−7218.
(39) Ro, I.; Qi, J.; Lee, S.; Xu, M.; Yan, X.; Xie, Z.; Zakem, G.; Morales, A.; Chen, J. G.; Pan, X.; Vlachos, D. G.; Caratzoulas, S.; Christopher, P. Bifunctional hydroformylation on heterogeneous Rh-WOx pair site catalysts. *Nature* **2022**, *609* (7926), 287−292.
(40) Yang, D.; Xu, P.; Browning, N. D.; Gates, B. C. Tracking Rh atoms in zeolite HY: First steps of metal cluster formation and influence of metal nuclearity on catalysis of ethylene hydrogenation and ethylene dimerization. *J. Phys. Chem. Lett.* **2016**, *7* (13), 2537−2543.
(41) Serna, P.; Gates, B. Zeolite-supported rhodium complexes and clusters: Switching catalytic selectivity by controlling structures of essentially molecular species. *J. Am. Chem. Soc.* **2011**, *133* (13), 4714−4717.
(42) Zhang, S. R.; Nguyen, L.; Liang, J. X.; Shan, J. J.; Liu, J. Y.; Frenkel, A. I.; Patlolla, A.; Huang, W. X.; Li, J.; Tao, F. Catalysis on singly dispersed bimetallic sites. *Nat. Commun.* **2015**, *6*, 7938−7948.
(43) Shan, J. J.; Li, M. W.; Allard, L. F.; Lee, S. S.; Flytzani-Stephanopoulos, M. Mild oxidation of methane to methanol or acetic acid on supported isolated rhodium catalysts. *Nature* **2017**, *551* (7682), 605.
(44) Babucci, M.; Fang, C.-Y.; Hoffman, A. S.; Bare, S. R.; Gates, B. C.; Uzun, A. Tuning the selectivity of single-site supported metal catalysts with ionic liquids. *ACS Catal.* **2017**, *7* (10), 6969−6972.
(45) Zhang, Q.; Gao, S.; Yu, J. Metal Sites in Zeolites: Synthesis, Characterization, and Catalysis. *Chem. Rev.* **2022**, DOI: 10.1021/acs.chemrev.2c00315.
(46) Qi, L.; Babucci, M.; Zhang, Y.; Lund, A.; Liu, L.; Li, J.; Chen, Y.; Hoffman, A. S.; Bare, S. R.; Han, Y. Propane Dehydrogenation Catalyzed by Isolated Pt Atoms in ≡SiOZn−OH Nests in Dealuminated Zeolite Beta. *J. Am. Chem. Soc.* **2021**, *143* (50), 21364−21378.
(47) Zhang, Y.; Qi, L.; Leonhardt, B.; Bell, A. T. Mechanism and Kinetics of *n*-Butane Dehydrogenation to 1,3-Butadiene Catalyzed by Isolated Pt Sites Grafted onto ≡SiOZn−OH Nests in Dealuminated Zeolite Beta. *ACS Catal.* **2022**, *12* (2022), 3333−3345.
(48) Zhang, Y.; Qi, L.; Lund, A.; Lu, P.; Bell, A. T. Mechanism and Kinetics of Acetone Conversion to Isobutene over Isolated Hf Sites Grafted to Silicalite-1 and SiO_2. *J. Am. Chem. Soc.* **2021**, *143* (22), 8352−8366.
(49) Qi, L.; Zhang, Y.; Conrad, M. A.; Russell, C. K.; Miller, J.; Bell, A. T. Ethanol Conversion to Butadiene over Isolated Zinc and Yttrium Sites Grafted onto Dealuminated Beta Zeolite. *J. Am. Chem. Soc.* **2020**, *142* (34), 14674−14687.

https://doi.org/10.1021/jacs.2c11075
J. Am. Chem. Soc. 2023, 145, 2911−2929

(50) Kots, P. A.; Zabilska, A. V.; Ivanova, I. I. Selective Self-Condensation of Butanal over Zr-BEA Zeolites. *ChemCatChem.* **2020**, *12* (1), 248−258.
(51) Sushkevich, V. L.; Vimont, A.; Travert, A.; Ivanova, I. I. Spectroscopic Evidence for Open and Closed Lewis Acid Sites in ZrBEA Zeolites. *J. Phys. Chem. C* **2015**, *119* (31), 17633−17639.
(52) Qi, L.; Zhang, Y.; Babucci, M.; Chen, C.; Lu, P.; Li, J.; Dun, C.; Hoffman, A. S.; Urban, J. J.; Tsapatsis, M. Dehydrogenation of Propane and *n*-Butane Catalyzed by Isolated $PtZn_4$ Sites Supported on Self-Pillared Zeolite Pentasil Nanosheets. *ACS Catal.* **2022**, *12*, 11177−11189.
(53) Wang, L.; Zhang, S.; Zhu, Y.; Patlolla, A.; Shan, J.; Yoshida, H.; Takeda, S.; Frenkel, A. I.; Tao, F. Catalysis and In Situ Studies of Rh_1/Co_3O_4 Nanorods in Reduction of NO with H_2. *ACS Catal.* **2013**, *3* (5), 1011−1019.
(54) Hoffman, A. S.; Fang, C.-Y.; Gates, B. C. Homogeneity of Surface Sites in Supported Single-Site Metal Catalysts: Assessment with Band Widths of Metal Carbonyl Infrared Spectra. *J. Phys. Chem. Lett.* **2016**, *7* (19), 3854−3860.
(55) Perez-Aguilar, J. E.; Chen, C.-Y.; Hughes, J. T.; Fang, C.-Y.; Gates, B. C. Isostructural Atomically Dispersed Rhodium Catalysts Supported on SAPO-37 and on HY Zeolite. *J. Am. Chem. Soc.* **2020**, *142* (26), 11474−11485.
(56) Camacho-Bunquin, J.; Aich, P.; Ferrandon, M.; Getsoian, A.; Das, U.; Dogan, F.; Curtiss, L. A.; Miller, J. T.; Marshall, C. L.; Hock, A. S.; Stair, P. C. Single-site zinc on silica catalysts for propylene hydrogenation and propane dehydrogenation: Synthesis and reactivity evaluation using an integrated atomic layer deposition-catalysis instrument. *J. Catal.* **2017**, *345*, 170−182.
(57) Takahashi, N.; Kobayashi, M. Comparison of ethylene with propylene hydroformylation over a Rh-Y zeolite catalyst under atmospheric pressure. *J. Catal.* **1984**, *85* (1), 89−97.
(58) Takahashi, N.; Matsuo, H.; Kobayashi, M. Kinetics and mechanism of ethylene hydroformylation over Rh-Y zeolite under atmospheric pressure. *J. Chem. Soc., Faraday Trans.* **1984**, *80* (3), 629−634.
(59) Arai, H.; Tominaga, H. Hydroformylation and hydrogenation of olefins over rhodium zeolite catalyst. *J. Catal.* **1982**, *75* (1), 188−189.
(60) Cavanagh, R.; Yates, J. T., Jr Site distribution studies of Rh supported on Al_2O_3—An infrared study of chemisorbed CO. *J. Chem. Phys.* **1981**, *74* (7), 4150−4155.
(61) Yates, J., Jr; Duncan, T.; Worley, S.; Vaughan, R. Infrared spectra of chemisorbed CO on Rh. *J. Chem. Phys.* **1979**, *70* (3), 1219−1224.
(62) Rice, C.; Worley, S.; Curtis, C.; Guin, J.; Tarrer, A. The oxidation state of dispersed Rh on Al_2O_3. *J. Chem. Phys.* **1981**, *74* (11), 6487−6497.
(63) Abreu, N. J.; Valdés, H.; Zaror, C. A.; Azzolina-Jury, F.; Meléndrez, M. F. Ethylene adsorption onto natural and transition metal modified Chilean zeolite: An operando DRIFTS approach. *Micropor. Mesopor. Mater.* **2019**, *274*, 138−148.
(64) Spoto, G.; Bordiga, S.; Ricchiardi, G.; Scarano, D.; Zecchina, A.; Borello, E. IR study of ethene and propene oligomerization on H-ZSM-5: hydrogen-bonded precursor formation, initiation and propagation mechanisms and structure of the entrapped oligomers. *J. Chem. Soc., Faraday Trans.* **1994**, *90* (18), 2827−2835.
(65) Geobaldo, F.; Spoto, G.; Bordiga, S.; Lamberti, C.; Zecchina, A. Propene oligomerization on H-mordenite: Hydrogen-bonding interaction, chain initiation, propagation and hydrogen transfer studied by temperature-programmed FTIR and UV−VIS spectroscopies. *J. Chem. Soc., Faraday Trans.* **1997**, *93* (6), 1243−1249.
(66) Moigno, D.; Callejas-Gaspar, B.; Gil-Rubio, J.; Werner, H.; Kiefer, W. The metal−carbon bond in vinylidene, carbonyl, isocyanide and ethylene complexes. *J. Organomet. Chem.* **2002**, *661* (1−2), 181−190.
(67) Haji, S.; Erkey, C. Investigation of rhodium catalyzed hydroformylation of ethylene in supercritical carbon dioxide by in situ FTIR spectroscopy. *Tetrahedron* **2002**, *58* (20), 3929−3941.
(68) Sivasankar, N.; Frei, H. Direct observation of kinetically competent surface intermediates upon ethylene hydroformylation over Rh/Al_2O_3 under reaction conditions by time-resolved Fourier transform infrared spectroscopy. *J. Phys. Chem. C* **2011**, *115* (15), 7545−7553.
(69) Chuang, S. S.; Pien, S.-I. Infrared spectroscopic studies of ethylene hydroformylation on Rh/SiO_2: An investigation of the relationships between homogeneous and heterogeneous hydroformylation. *J. Mol. Catal.* **1989**, *55* (1), 12−22.
(70) Chen, L.; Zhu, Y.; Zheng, H.; Zhang, C.; Li, Y. Aqueous-phase hydrodeoxygenation of propanoic acid over the Ru/ZrO_2 and Ru−Mo/ZrO_2 catalysts. *Appl. Catal. A: Gen.* **2012**, *411*, 95−104.
(71) Deeming, A.; Shaw, B. Some phosphine exchange and oxidative addition reactions of complexes of the type trans-$[RhX(CO)L_2]$(X = Halide; L = dimethylphenyl-phosphine or-arsine). *J. Chem. Soc: Inorganic, Physical, Theoretical* **1969**, 597−602.
(72) Bennett, M.; Jeffery, J.; Robertson, G. Oxidative addition of acyl chlorides to chlorotris (dimethylphenylphosphine) complexes of rhodium (I) and iridium (I). Crystal and molecular structure of $[RhCl(COCH_3)(PMe_2Ph)_3]PF_6$, an acetyl complex which undergoes unusually fast methyl migration in solution. *Inorg. Chem.* **1981**, *20* (2), 323−330.
(73) Chutia, P.; Sarmah, B. J.; Dutta, D. K. Oxidative addition of different electrophiles with rhodium (I) carbonyl complexes of unsymmetrical phosphine−phosphine monoselenide ligands. *Appl. Org. Chem.* **2006**, *20* (8), 512−520.
(74) Derecskei-Kovacs, A.; Marynick, D. S. A new look at an old reaction: The potential energy surface for the thermal carbonylation of $Mn(CO)_5CH_3$. The role of two energetically competitive intermediates on the reaction surface, and comments on the photodecarbonylation of $Mn(CO)_5(COCH_3)$. *J. Am. Chem. Soc.* **2000**, *122* (9), 2078−2086.
(75) Hadjiivanov, K. I.; Vayssilov, G. N. Characterization of oxide surfaces and zeolites by carbon monoxide as an IR probe molecule. *Adv. Catal.* **2002**, *47*, 307−511.
(76) Tang, Y.; Asokan, C.; Xu, M.; Graham, G. W.; Pan, X.; Christopher, P.; Li, J.; Sautet, P. Rh single atoms on TiO_2 dynamically respond to reaction conditions by adapting their site. *Nat. Commun.* **2019**, *10* (1), 4488.
(77) Hwang, K. S.; Yang, M.; Zhu, J.; Grunes, J.; Somorjai, G. A. The molecular mechanism of the poisoning of platinum and rhodium catalyzed ethylene hydrogenation by carbon monoxide. *J. Mol. Catal. A: Chem.* **2003**, *204*, 499−507.
(78) Rioux, R. M.; Hoefelmeyer, J. D.; Grass, M.; Song, H.; Niesz, K.; Yang, P.; Somorjai, G. A. Adsorption and co-adsorption of ethylene and carbon monoxide on silica-supported monodisperse Pt nanoparticles: volumetric adsorption and infrared spectroscopy studies. *Langmuir* **2008**, *24* (1), 198−207.
(79) Rioux, R. M.; Komor, R.; Song, H.; Hoefelmeyer, J. D.; Grass, M.; Niesz, K.; Yang, P.; Somorjai, G. A. Kinetics and mechanism of ethylene hydrogenation poisoned by CO on silica-supported monodisperse Pt nanoparticles. *J. Catal.* **2008**, *254* (1), 1−11.
(80) Liu, J.; Yan, L.; Ding, Y. J.; Jiang, M.; Dong, W. D.; Song, X. E.; Liu, T.; Zhu, H. J. Promoting effect of Al on tethered ligand-modified Rh/SiO_2 catalysts for ethylene hydroformylation. *Appl. Catal. A-Gen.* **2015**, *492*, 127−132.
(81) Hanh, N. T. H.; Duc, D. T.; Dao, T. V.; Le, M. T.; Riisager, A.; Fehrmann, R. Characterization and parametrical study of Rh-TPPTS supported ionic liquid phase (SILP) catalysts for ethylene hydroformylation. *Catal. Commun.* **2012**, *25*, 136−141.
(82) Li, X. M.; Ding, Y. J.; Jiao, G. P.; Li, J. W.; Lin, R. H.; Gong, L. F.; Yan, L.; Zhu, H. J. A new concept of tethered ligand-modified Rh/SiO_2 catalyst for hydroformylation with high stability. *Appl. Catal. A-Gen.* **2009**, *353* (2), 266−270.
(83) Balakos, M. W.; Chuang, S. S. Dynamic and LHHW kinetic analysis of heterogeneous catalytic hydroformylation. *J. Catal.* **1995**, *151* (2), 266−278.

https://doi.org/10.1021/jacs.2c11075
J. Am. Chem. Soc. 2023, 145, 2911−2929

(84) Balakos, M. W.; Chuang, S. S. Transient response of propionaldehyde formation during $CO/H_2/C_2H_4$ reaction on Rh/SiO_2. *J. Catal.* **1995**, *151* (2), 253−265.
(85) Heck, R. F.; Breslow, D. S. The reaction of cobalt hydrotetracarbonyl with olefins. *J. Am. Chem. Soc.* **1961**, *83* (19), 4023−4027.
(86) Sparta, M.; Børve, K. J.; Jensen, V. R. Activity of rhodium-catalyzed hydroformylation: Added insight and predictions from theory. *J. Am. Chem. Soc.* **2007**, *129* (27), 8487−8499.
(87) Chen, S.; Zhao, Z.-J.; Mu, R.; Chang, X.; Luo, J.; Purdy, S. C.; Kropf, A. J.; Sun, G.; Pei, C.; Miller, J. T. Propane Dehydrogenation on Single-Site $[PtZn_4]$ Intermetallic Catalysts. *Chem.* **2021**, *7* (2), 387−405.
(88) Oswald, A.; Hendrikse, D.; et al. *Phosphorus Sulfur* **1987**, *30*, 237−240.
(89) MacDougall, J. K.; Simpson, M. C.; Green, M. J.; Cole-Hamilton, D. J. Direct formation of alcohols by hydrocarbonylation of alkenes under mild conditions using rhodium trialkylphosphine catalysts. *J. Chem. Soc., Dalton Trans.* **1996**, *6*, 1161−1172.
(90) Moser, W. R.; Papile, C. J.; Brannon, D. A.; Duwell, R. A.; Weininger, S. J. The mechanism of phosphine-modified rhodium-catalyzed hydroformylation studied by CIR-FTIR. *J. Mol. Catal.* **1987**, *41* (3), 271−292.
(91) Unruh, J. D.; Christenson, J. R. A study of the mechanism of rhodium/phosphine-catalyzed hydroformylation: use of 1,1′-bis (diarylphosphino) ferrocene ligands. *J. Mol. Catal.* **1982**, *14* (1), 19−34.
(92) Buhling, A.; Kamer, P. C.; van Leeuwen, P. W. Rhodium catalysed hydroformylation of higher alkenes using amphiphilic ligands. *J. Mol. Catal. A: Chem.* **1995**, *98* (2), 69−80.
(93) Janecko, H.; Trzeciak, A. M.; Ziółkowski, J. J. New rhodium complexes as low pressure hydroformylation catalysts: effect of ligand on catalyst activity and selectivity. *J. Mol. Catal.* **1984**, *26* (3), 355−361.
(94) Van Rooy, A.; de Bruijn, J. N.; Roobeek, K. F.; Kamer, P. C.; Van Leeuwen, P. W. Rhodium-catalysed hydroformylation of branched 1-alkenes; bulky phosphite vs. triphenylphosphine as modifying ligand. *J. Organomet. Chem.* **1996**, *507* (1−2), 69−73.
(95) Christiansen, A.; Li, C.; Garland, M.; Selent, D.; Ludwig, R.; Franke, R.; Börner, A. Secondary Phosphane Oxides as Preligands in Rhodium-Catalyzed Hydroformylation. *ChemCatChem.* **2010**, *2* (10), 1278−1285.
(96) Bortenschlager, M.; Schütz, J.; von Preysing, D.; Nuyken, O.; Herrmann, W. A.; Weberskirch, R. Rhodium−NHC-complexes as potent catalysts in the hydroformylation of 1-octene. *J. Organomet. Chem.* **2005**, *690* (24−25), 6233−6237.
(97) Liu, G.; Volken, R.; Garland, M. Unmodified rhodium-catalyzed hydroformylation of alkenes using tetrarhodium dodeca-carbonyl. The infrared characterization of 15 acyl rhodium tetracarbonyl intermediates. *Organometallics* **1999**, *18* (17), 3429−3436.
(98) Feng, J.; Garland, M. Unmodified homogeneous rhodium-catalyzed hydroformylation of styrene. The detailed kinetics of the regioselective synthesis. *Organometallics* **1999**, *18* (3), 417−427.
(99) Garland, M.; Pino, P. Kinetics of the formation and hydrogenolysis of acylrhodium tetracarbonyl. *Organometallics* **1991**, *10* (6), 1693−1704.
(100) Joly, J.; Zanier-Szydlowski, N.; Colin, S.; Raatz, F.; Saussey, J.; Lavalley, J. Infrared in situ characterization of HY zeolite acid sites during cyclohexene transformation. *Catal. Today* **1991**, *9* (1−2), 31−38.
(101) Newville, M.; Ravel, B. ATHENA, ARTEMIS, HEPHAESTUS: data analysis for X-ray absorption spectroscopy using IFEFFIT. *J. Synchrotron Radiat.* **2005**, *12* (4), 537−541.

https://doi.org/10.1021/jacs.2c11075
J. Am. Chem. Soc. 2023, 145, 2911−2929